The Thesis Committee for Andrew Joseph Nicholson
Certifies that this is the approved version of the following thesis:

Empirical Analysis of Fault Seal Capacity for CO_2 sequestration, Lower Miocene, Texas Gulf Coast

APPROVED BY
SUPERVISING COMMITTEE:

Supervisor:

Scott W. Tinker

Co-Supervisor:

Timothy A. Meckel

Ramon H. Trevino

Ronald J. Steel

Empirical Analysis of Fault Seal Capacity for CO_2 Sequestration, Lower Miocene, Texas Gulf Coast

by

Andrew Joseph Nicholson, B.S.Geo.Sci.

Thesis

Presented to the Faculty of the Graduate School of

The University of Texas at Austin

in Partial Fulfillment

of the Requirements

for the Degree of

Master of Science in Geological Sciences

The University of Texas at Austin

May, 2012

Dedication

This work is dedicated to my family, fiancé, friends, and mentors.

Acknowledgements

I would like to thank my supervisor, Scott Tinker, for supporting our research group and agreeing to give his time to assist me and offer advice and constructive criticism, my committee members and research supervisors, Tip Meckel and Ramon Trevino, for their constant support, education, and belief in me, and my final committee member and former undergraduate supervisor, Ron Steel, for his time educating me and providing a strong foundation in siliciclastic sedimentary geology. I am forever grateful to all of you.

I would like to thank Scott Wilkins for his patience and original teachings on the fundamentals of subsurface membrane fault seal analysis. Thank you for everything. I am also appreciative of the support and teachings from the rest of the Miocene Megatransect researchers and students (David Carr, Jiemin Lu, Erin Miller, Kerstan Wallace, Julie Ditkof, and Brandon Johnson).

I would also like to thank the Gulf Coast Carbon Center researchers and its director, Sue Hovorka, for their support and time offered to me over the years in the form of endless answered questions. To all my teachers over the past six years of undergraduate and graduate school, I am deeply appreciative of your commitment to students of the Jackson School of Geosciences. Special thanks to the Information Technology department at the Bureau of Economic Geology for keeping my software running and data in order. They were an integral part of daily research life.

Thank you to Badleys Geoscience Limited for the use of their TrapTester software, to Landmark, Kingdom SMT, and IHS Petra for use of their well log and seismic interpretation software, to ION Geophysical for access to the 2D GulfSPAN

seismic data, to Neumin Production for access to their Lavaca Bay 3D seismic data, and to Seismic Exchange, Inc. for their support of our research efforts.

The Jackson School of Geosciences generously supported me over the years in the form of scholarships and a TA position. The DOE directly funded my education through GRA positions in support of our Miocene research.

Finally, and most importantly, I would like to thank my family and my fiancé for their love and support.

Abstract

Empirical Analysis of Fault Seal Capacity for CO_2 Sequestration, Lower Miocene, Texas Gulf Coast

Andrew Joseph Nicholson, M.S.Geo.Sci.

The University of Texas at Austin, 2012

Supervisors: Scott W. Tinker, Timothy A. Meckel

The Gulf Coast of Texas has been proposed as a high capacity storage region for geologic sequestration of anthropogenic CO_2. The Miocene section within the Texas State Waters is an attractive offshore alternative to onshore sequestration. However, the stratigraphic targets of interest highlight a need to utilize fault-bounded structural traps. Regional capacity estimates in this area have previously focused on simple volumetric estimations or more sophisticated fill-to-spill scenarios with faults acting as no-flow boundaries. Capacity estimations that ignore the static and dynamic sealing capacities of faults may therefore be inaccurate. A comprehensive fault seal analysis workflow for CO_2-brine membrane fault seal potential has been developed for geologic site selection in the Miocene section of the Texas State Waters. To reduce uncertainty of fault performance, a fault seal calibration has been performed on 6 Miocene natural gas traps in the Texas State Waters in order to constrain the capillary entry pressures of the modeled fault gouge. Results indicate that modeled membrane fault seal capacity for the

Lower Miocene section agrees with published global fault seal databases. Faults can therefore serve as effective seals, as suggested by natural hydrocarbon accumulations. However, fault seal capacity is generally an order of magnitude lower than top seal capacity in the same stratigraphic setting, with implications for storage projects. For a specific non-hydrocarbon producing site studied for sequestration (San Luis Pass salt dome setting) with moderately dipping (16°) traps (i.e. high potential column height), membrane fault seal modeling is shown to decrease fault-bound trap area, and therefore storage capacity volume, compared with fill-to-spill modeling. However, using the developed fault seal workflow at other potential storage sites will predict the degree to which storage capacity may approach fill-to-spill capacity, depending primarily on the geology of the fault (shale gouge ratio – SGR) and the structural relief of the trap.

Table of Contents

List of Figures xi

Introduction 1

Regional Geology 3

Prospective Sequestration Plays and Fault Distribution 7

Factors Limiting Hydrocarbon Accumulation: Seal Capacity 9

- Structural Spill & Juxtaposition Leak 9
- Capillary Fault Seal and Top Seal 10
- Mechanical Top Seal Failure and Fault Reactivation Leakage 10

Fault Rock Types and Determination 13

- Cataclasites & Disaggregation Zones 13
- Phyllosilicate Framework Fault Rocks 14
- Shale Smears 14

Fault Seal Prediction in the Subsurface – the Shale Gouge Ratio 16

Buoyancy Pressure and Capillary Entry Pressure 20

Fluid Properties and Their Effect On Capillary Entry Pressure 23

- Temperature & Pressure 23
- Fluid Density 24
- Interfacial Tension 26
- Salinity 28
- Contact Angle 30
- Mercury-Air Normalization 30

Calibrating the Quantitative Fault Seal Failure Envelope 32

- The Global Fault Seal Database 32
- Fault Seal Calibration Workflow for Historic Natural Gas Fields 35
- Calibration Results 37

Fault Seal Variation with Depth 41

Modeling Membrane Fault Seal for a Potential Sequestration Prospect 44

Static CO2-Brine Membrane Fault Seal Workflow Summary 48

Fault Seal Capacity vs Fill-to-Spill Capacity.....49

Fault Slip Stability 51

Variability in the SGR Calculation – Sources of Error and Cause for Concern....56

V_{cl} Calibration 56

Lateral Stratigraphic Heterogeneity.....56

Structural Interpretation From Seismic.....56

Seismic Resolution and the Fault Damage Zone 57

Small Throw on Faults.....58

Discussion 60

New Data Contributions 63

Conclusions.....64

Appendix A.....66

Appendix B 67

Appendix C 72

Appendix D.....76

References.....78

List of Figures

Figure 1. Data and figure locations, upper Texas Gulf Coast 5

Figure 2. Dip-oriented structural cross section 6

Figure 3. Structure, faulting, and natural gas accumulations of the Lower Miocene 8

Figure 4. Mechanisms that limit natural accumulations 12

Figure 5. Fault rock types 15

Figure 6. Deterministic fault seal literature review 17

Figure 7. Shale gouge ratio (SGR) 18

Figure 8. Qualitative use of the SGR 19

Figure 9. Hypothetical buoyancy pressure 22

Figure 10. Capillary entry schematic 22

Figure 11. Temperature, pressure, density, and interfacial tension trends with depth 25

Figure 12. Ratio of CO_2-brine density in equilibrium and pure CO_2 density vs. pressure for varying reservoir scale temperatures 29

Figure 13. Global fault seal calibration database 34

Figure 14. Structure map of the Brazos Block 440 B sand 36

Figure 15. Triangle diagram for the Brazos Block 440 B sand 39

Figure 16. Calibrated Lower Miocene fault seal & top seal 40

Figure 17. Fault bound column heights trends with depth 43

Figure 18. San Luis Pass salt dome, LM2 structure map, SE fault block 45

Figure 19. Gamma ray well log type section for the Lower Miocene 1 & 2, San Luis Pass. 46

Figure 20. Buoyancy pressure profile schematic 47
Figure 21. Schematic 3-dimensional fault modeling workflow 47
Figure 22. Buoyancy pressure profile LM2, SE fault block, San Luis Pass salt dome 50
Figure 23. Fault slip stability schematic 52
Figure 24. Regional fault strike rose diagram 53
Figure 25. Fault slip stability plots for the A Fault and B Fault 54
Figure 26. Fault trace length vs maximum fault throw, LM2 horizon. 58

Introduction

The Texas Gulf Coast contains many point sources of anthropogenic carbon dioxide (CO_2) emissions such as refineries, petrochemical plants, coal and natural gas power plants, and cement factories. In addition, the region exemplifies both historic and active hydrocarbon exploration, which provides abundant data on the local stratigraphy that can be used for carbon sequestration. The thick (5,000 – 15,000') clastic Miocene section, with porous (>25% porosity) reservoirs and numerous regional seals, is available for commercial CO_2 sequestration or enhanced oil recovery (EOR) operations in the State Waters of Texas. The State Waters provide a common lessor for mineral ownership and the lack of potable groundwater resources mitigates the risk of USDW (Underground Source of Drinking Water) contamination. Shallow water depth (<100') can aid surface monitoring efforts (von Deimling et al., 2010). Data from natural gas fields in Miocene reservoirs can be used as analogs prior to site selection for brine storage. An estimated 2.5 Gt or greater capacity resides in Gulf Coast EOR candidate fields (Holtz et al., 2005), while annual CO_2 emissions from the Gulf Coast region (Texas, Louisiana, and Mississippi) are ~1Gt per year (Ambrose et al., 2009). Thus, although EOR offers a needed early economic driver for CO_2 capture, compression, and transmission, brine storage will eventually need to be utilized to achieve long-term significant reduction in Gulf Coast emissions through time. CO_2 sequestration also has applications in tertiary EOR projects in which excess anthropogenic CO_2 may need to be stored in saline aquifers above or below the EOR zone.

Capacity estimation is a critical aspect of both local and regional sequestration site selection. Bradshaw et al. (2007) point out that many studies have focused on estimating regional capacity using simple pore-volume calculations. More advanced calculations use no-flow boundary conditions for faults and evaluate structural fill-to-spill capacity (Nicot et al., 2006). While treating faults as no-flow boundaries may be sufficient for first attempts at regional capacity estimates, site specific capacity estimates must consider the petrophysical properties of faults and their effect on CO_2 capacity over geologic time scales. Could fill-to-spill capacity modeling estimates, which represent the upper threshold of potential CO_2 storage capacity, be too high? Are we over predicting the long term CO_2 capacity of faulted basins? Historic natural gas field data in Miocene age reservoirs within the State Waters (Seni et al., 1997) provide natural analog data to perform empirical fault seal calibration that can be used in both regional and site specific CO_2 storage capacity estimates for fault-bound traps.

Membrane fault seal capacity modeling is hypothesized to lower estimates of CO_2 storage capacity when compared with fill-to-spill capacity modeling. In order to assess the relative importance of CO_2 fault seal capacity, regional fluid property trends are assessed, fault bound natural gas accumulations are calibrated with estimated fault rock properties, fault seal capacity is compared with top seal capacity from the same stratigraphic section, and a workflow is developed to empirically estimate the effect of membrane fault seal capacity compared with fill-to-spill capacity over geologic time scales.

Regional Geology

This study focuses on the Texas State Waters within the 10 mile wide tract of submerged land paralleling the Texas coastline (Figure 1). Data available for analysis include a Seismic Exchange, Inc. (SEI) 3D seismic dataset, ION Geophysical GulfSPAN 2D seismic data, synthetic seismograms and check shot surveys (Appendix A), and numerous well log and paleontological databases.

The present day Gulf of Mexico is a passive margin created by seafloor spreading during the Middle Jurassic through Early Cretaceous. Late Cretaceous through Paleocene Laramide basin formation across the Inner Cretaceous Seaway initiated high potential sediment yield within internal drainages in Wyoming, Colorado, and New Mexico, effectively starving the Northern Gulf of Mexico sediment supply. This initial meager sediment supply resulted in mixed carbonate and siliciclastic deposition in the Gulf of Mexico region. After many of the Laramide basins were filled in the latest Cretaceous and Paleocene, spillways developed and drainages gathered so that, from late Paleocene, high sediment volume rates (>100,000 km^3/Ma) entered the Northern Gulf of Mexico basin and terrigenous clastic wedges prograded basinward to the southeast. This drainage system from the northwest, as well as others from the north and northeast, continued to reach the Gulf waters through the Pleistocene (Galloway et al., 2011). The Lower Miocene interval of the Northwestern Gulf of Mexico formed two porous, siliciclastic progradational wedges that are available for CO_2 sequestration within the Texas State Waters (Figure 2). The regressive Lower Miocene 1 (LM1) and Lower Miocene 2 (LM2)

siliciclastic wedges that extend seaward from the Texas coastline are underlain by a major transgressive flooding surface represented lithologically by the late Oligocene Anahuac shale (Rainwater, 1964; Galloway, 1989). The thick (>1000') Anahuac section that strikes parallel to the present day coastline is downthrown thousands of feet by the Clemente-Tomas fault system, a Lower Miocene, linked growth fault succession (Galloway, 1989; Bradshaw and Watkins, 1994; McDonnell et al., 2009). Along the southern half of the Texas coastline these growth faults are caused by deltaic sand-loading and shelf-edge foundering of the mobile Anahuac shale (Winker and Edwards, 1983). The northern half of the growth fault succession paralleling the Texas coastline and into Louisiana is caused by evacuation of allocthonous salt (presumably Louann salt) from the previous Late Oligocene Anahuac shelf edge (McDonnell et al., 2009). The shale and salt evacuation along the Clemente-Tomas growth fault system resulted in a more than threefold increase in the hanging wall sediment thickness relative to the footwall of the LM1 in some localities (Figure 2). Growth faulting ceased by the LM2 regressive episode of shelf growth, allowing progradation of the shelf margin farther to the southeast and into the Corsair growth fault trend (Bradshaw and Watkins, 1994).

The Galloway (1989) classification scheme is used to distinguish the top LM1 and the top LM2 regressive episodes based on benthic foraminifera data. The *Marginulina ascensionensis* (Marg. A.) shale defines the top of the LM1 depositional episode and the *Amphistegina chipolensis* (Amph. B) shale defines the top of the LM2 depositional episode. The entire Lower Miocene succession spans in age from roughly 24-16 Ma

(Galloway, 1989). Both the LM1 and LM2 intervals provide prospective reservoirs and seals for CO_2 sequestration within the Texas State Waters.

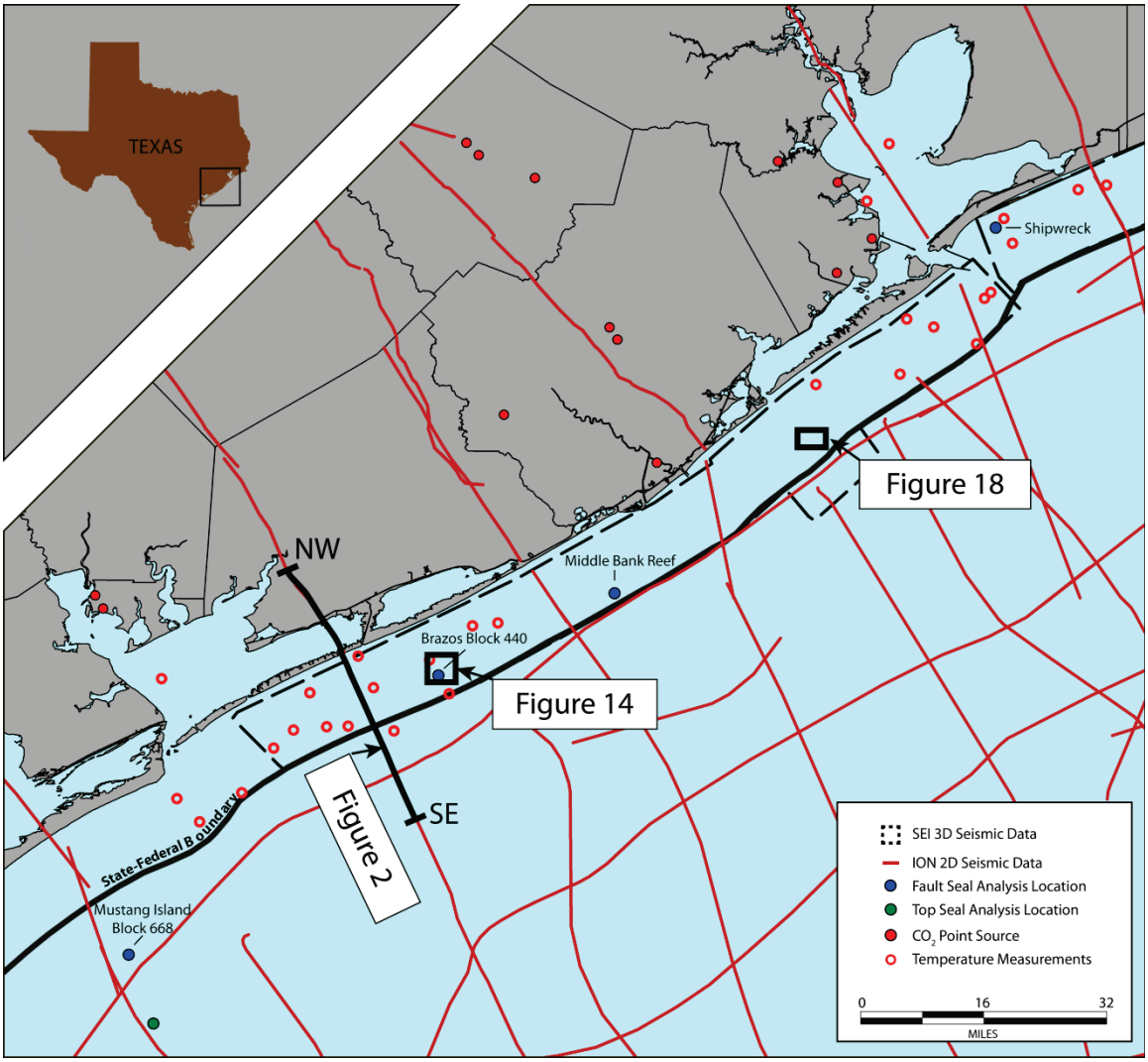

Figure 1. Data and figure locations, upper Texas Gulf Coast.

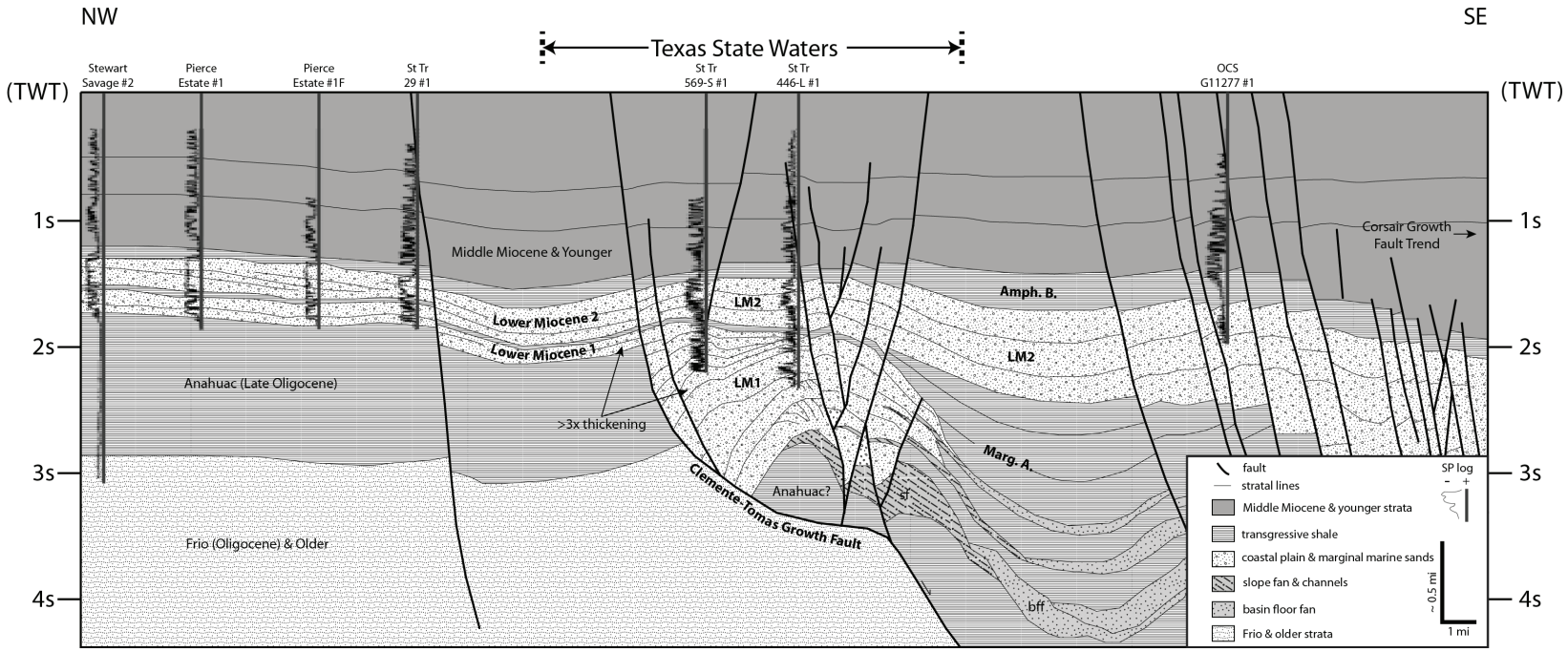

Figure 2. Dip-oriented structural cross section. Interpreted from ION 2D geophysical line. Location shown in Fig. 1.

Prospective Sequestration Plays and Fault Distribution

While there is considerable pore space available for CO_2 sequestration in Miocene brine reservoirs in the Texas State Waters, many sub-regional (site scale) structural boundaries exist (e.g. faults). A structure map of the top of the Lower Miocene 2 indicates that fault surfaces mapped in seismic data bound even the largest potential sites and often cut through structural highs (Figure 3A). Prospective sequestration sites for the LM2 horizon are growth-faulted shelf-edge rollover anticlines, transverse grabens, faulted syncline mini-basins, and piercement salt domes. The transverse grabens are formed from corrugations in the Clemente-Tomas fault system inherited from previous Oligocene detachments (Trevino and Vendeville, 2008; McDonnell et al., 2010). For the LM1 horizon the dominant play type is rollover anticlines formed during the regional growth faulting phase of the Clemente-Tomas linked growth fault (McDonnell et al., 2010). Existing natural gas fields from the Lower Miocene 2 and the upper portion of the Lower Miocene 1 conform to structure rather than stratigraphy (Figure 3B). This suggests that understanding fault seal, regardless of the play type chosen, is critical.

Near-surface (sea floor) penetrating faults (Figure 3C) extend to the upper limits of seismic resolution (< 0.3s, or < ~850 ft) and are a concern for CO_2 storage in that they provide a potential leakage pathway to the sea floor. It is known that faults can act as both seals and conduits for fluid (Weber et al., 1978; Bouvier et al., 1989; Alexander and Handschy, 1998; Davies et al., 2003). Even though it is highly unlikely that fault parallel flow (i.e. vertically and laterally along a fault, as opposed to across-fault flow) would

occur in a continuous leak from the injection interval to the surface, faults can cause leakage out of a purported containment structure if they are not sealing. A fault seal calibration is necessary to understand both the degree to which faults are sealing and the petrophysical properties of the sealing fault-rock.

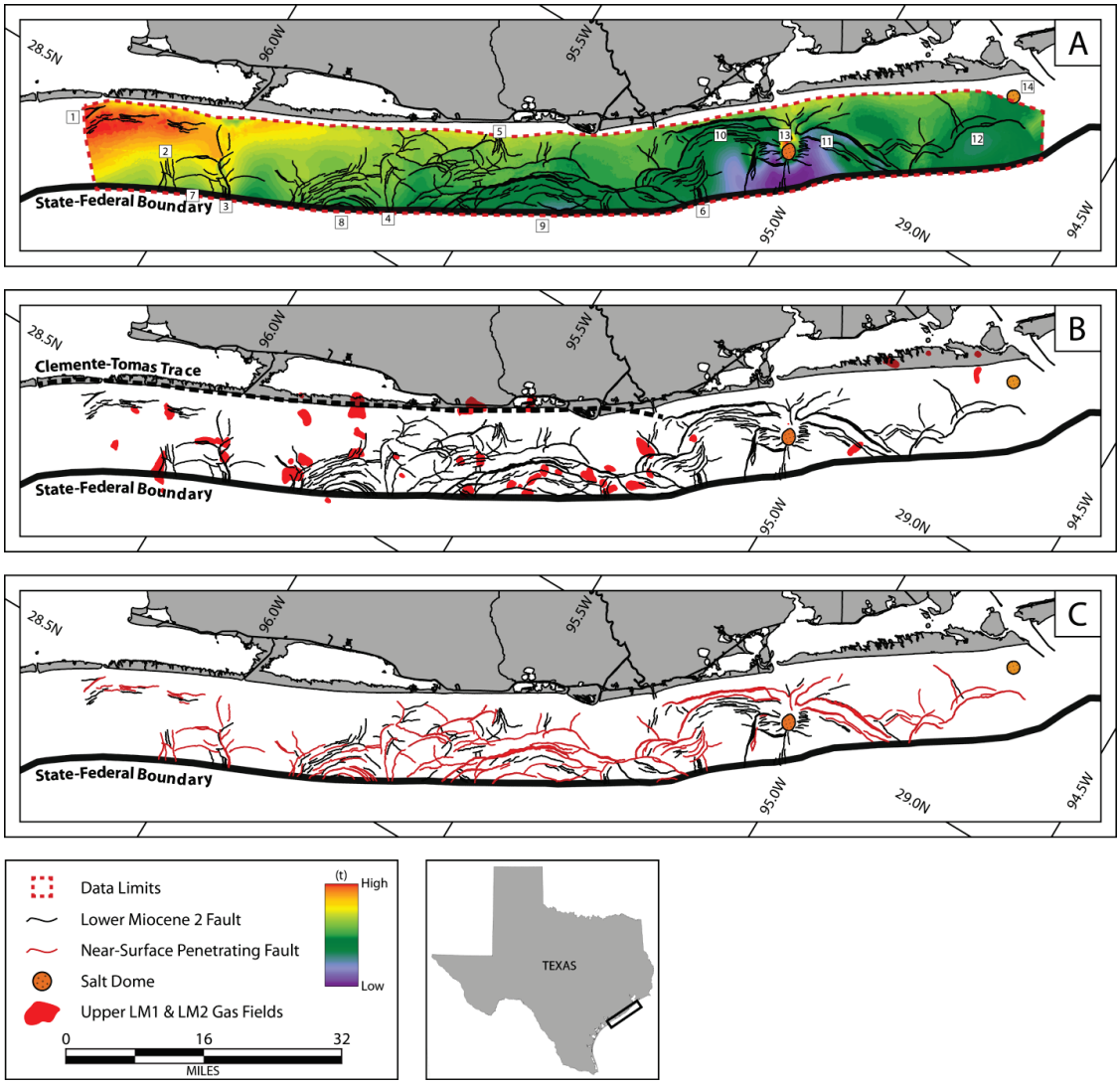

Figure 3. Structure, faulting, and natural gas accumulations of the Lower Miocene. (A) Time structure map and sequestration play types for the LM2: (1) rollover anticlines; (2-6) transverse grabens; (7-12) faulted synclinal minibasins; (13-14) piercement salt domes. (B) LM2 fault polygons overlain with upper LM1 and LM2 gas field polygons. (C) 'Near-seafloor' penetrating faults outlined with red fault polygons.

Factors Limiting Hydrocarbon Accumulation: Seal Capacity

Faults can represent important boundaries for fluid entrapment and it is important to understand the broad categories of mechanisms that can limit the size of a trapped fluid accumulation (Yielding et al., 2010) over both geologic time scales (thousands of years) and sequestration time scales (decades to centuries). Buoyancy force created between the less dense immiscible hydrocarbon (non-wetting phase) and brine (wetting phase) is the dominant mechanism driving secondary migration (both lateral and vertical) of hydrocarbons (Thomas et al., 1968; Schowalter, 1979). The main mechanisms limiting hydrocarbon accumulation size are structural spill and faulted self-juxtaposition of reservoir sands, top seal and fault seal capillary entry pressure (Schowalter, 1979), and top seal and fault seal mechanical failure (Handin et al., 1963; Jaeger and Cook, 1969). The fault seal mechanisms are considered with details presented below (Figure 4). Specific equations governing the limiting factors will be covered in later chapters on fault rock properties, buoyancy pressure, capillary entry pressure, and fluid properties.

STRUCTURAL SPILL & JUXTAPOSITION LEAK

Structural spill of any trap is the basic and simplest limiting factor for any buoyant fluid displacing brine. Structural spill occurs when the buoyant fluid fills the entire structural relief of the trap and the trap cannot hold any more buoyant fluid. Juxtaposition spill occurs when the trapped fluid fills to the tip of a fault (zero displacement point), or where the reservoir regains self-juxtaposition (Allan, 1989), but the structural spill could still hold more buoyant fluid (Figure 4A). Across-fault

juxtaposition of sand-on-sand or sand-on-shale does not necessarily mean those contacts are leak points or seals, respectively. Fault rock (or fault gouge) material will exist between the juxtaposition, and this will determine the degree of seal or lack thereof.

CAPILLARY FAULT SEAL AND TOP SEAL

Capillary (membrane) fault seal and top seal (Figure 4B) become a potential controlling factor when traps are not filled to either the structural spill or the juxtaposition leak point (Schowalter, 1979). In the case that fault seal or top seal are the limiting factor, capillary entry pressure (P_{ce}) of the top seal lithology or fault rock determines the maximum supported column height. Traps in which fluids have exceeded the capillary entry pressure of the seals will remain sealing once enough fluid has migrated out of the trap to regain equilibrium capillary pressures (Thomas et al., 1968), i.e. when the buoyancy pressure (BP) is once again below the capillary entry pressure.

MECHANICAL TOP SEAL FAILURE AND FAULT REACTIVATION LEAKAGE

Fracturing of the reservoir and top seal can occur (Figure 4C) if the total pore pressure, or reference pore pressure (RPP, equal to or greater than hydrostatic pore pressure) plus buoyancy pressure, exceeds the minimum principal horizontal stress (S_h). Pore pressure limits from a South Texas study of overpressured oil and gas fields by Engelder and Leftwich Jr. (1997), particularly from Oligocene (Frio) examples in the Redfish Bay area, show that pore pressure never exceeded values of 80-90% of lithostatic stress (S_v), providing an approximation for S_h. The Engelder and Leftwich Jr. (1997)

study provides a good methodology for estimating S_h in the absence of leakoff tests by using existing pore pressure data.

Preexisting faults can also reactivate (Figure 4C) at lower pore pressures (the critical pore pressure, S_c) than required to hydraulically fracture the top seal (Finkbeiner et al., 2001). Leakage by fault reactivation has been documented in field studies (Wiprut and Zoback, 2000; Lyon et al., 2005), but it is difficult to distinguish from leakage by hydraulic fracturing. Fault reactivation occurs when the total pore pressure causes the differential principal stresses to intersect the Mohr-Coulomb failure envelope of a preexisting fault (Finkbeiner et al., 2001). Reactivation will be covered in a later chapter. Because fault reactivation and hydraulic fracturing of the reservoir are limiting factors for CO_2 sequestration that can be addressed with pressure management and modeled for the short-term injection time scales, long term storage of CO_2 adjacent to faults requires focusing on fault seal and top seal capillary entry pressures.

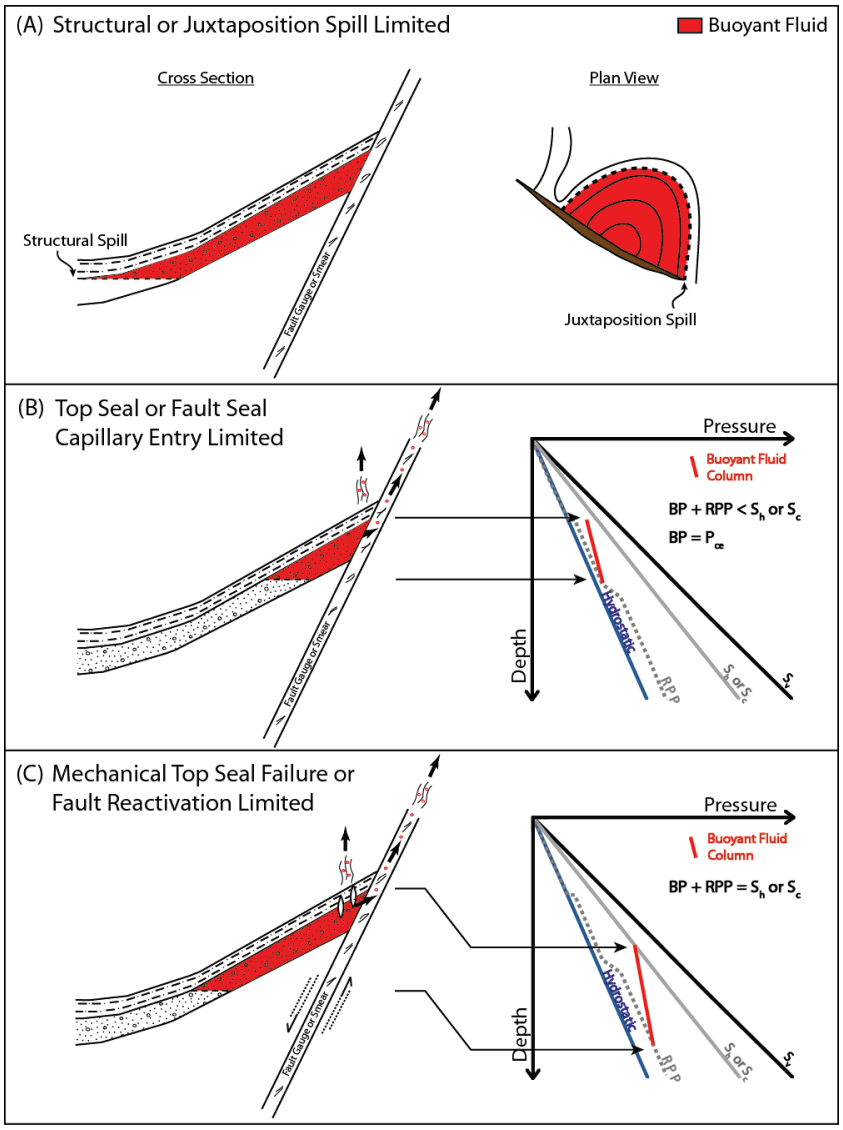

Figure 4. Mechanisms that limit natural accumulations. (A) Structural and self-juxtaposition spill limited. (B) Top seal or fault seal capillary entry limited. When the buoyancy pressure (BP) equilibrates to the capillary entry pressure (P_{ce}) of the fault rock or top seal, but the reference pore pressure (RPP; or overpressured brine) and buoyancy pressure does not exceed the depth equivalent minimum principal horizontal stress (S_h; or fracture gradient) or critical stress (S_c; or fault reactivation pressure). (C) Mechanical top seal failure (BP+RPP=S_h) or fault reactivation (BP+RPP=S_c) limited.

Fault Rock Types and Determination

Fault gouge in clastic sedimentary systems, much like its host rock, shows variations in both lithology and petrophysical properties. Before assessing the prediction of fault rock lithology and petrophysical properties in the subsurface it is important to understand the main categories of fault rock as summarized in Fisher and Knipe (1998). Outcrop and thin section photographs (Figure 5) illustrate the fault rock classification (Yielding et al., 2010).

CATACLASITES & DISAGGREGATION ZONES

Cataclasites occur in porous, clay free sandstones during faulting (Fisher and Knipe, 1998) and are often referred to as deformation bands. Deformation bands form as single shear bands (mm to cm scale width), evolve into zones of deformation bands, and may eventually result in a slip plane (Antonellini and Aydin, 1994). These bands are the result of grain crushing, rotation, and sliding due to mechanical compaction at grain-to-grain contacts (Milliken and Reed, 2002). Cataclasis results in loss of permeability and porosity relative to the host rock from which they were formed due to both mechanical and enhanced chemical compaction (Antonellini and Aydin, 1994; Milliken and Reed, 2002).

Disaggregation zones are similar to cataclasites, with throws on the order of millimeters to centimeters, but are formed under low mean effective stress conditions (either shallow burial or low effective stress while lacking cementation) and therefore do not involve grain crushing (Sperrevik et al., 2002).

PHYLLOSILICATE FRAMEWORK FAULT ROCKS

Phyllosilicate Framework Fault Rocks (PFFR) are classified as having 15-40% phyllosilicates (e.g. chlorite, illite, smectite, kaolinite, etc.) and form by deformation induced mixing of impure (clay content >0%) sandstones and siltstones (Fisher and Knipe, 1998). PFFRs have been documented in Gulf of Mexico strata as old as Eocene (Smith, 1980; Berg and Avery, 1995), and based on data introduced in a later chapter, are the dominant sealing fault rock type for the Texas Gulf Coast Miocene strata.

SHALE SMEARS

Shale smears are continuous zones of ductilely deformed clay-rich host rock (>40% phyllosilicates) entrained parallel to the fault (Fisher and Knipe, 1998). Shale smear length and continuity is proportional to the source bed thickness and inversely proportional to the amount of throw along the fault. Mechanisms for shale smearing include abrasion of clay grains by juxtaposed sandstone during faulting, shearing, and to a lesser extent, injection of shale beds along the fault (Lindsay et al., 1993). Takahashi (2003) advanced the understanding of shale smear continuity through lab experiments by showing that the ratio of fault throw to source bed thickness required to maintain continuous smears increases with increasing effective normal stress. Therefore, in normal stress regimes, as depth increases without an increase in overpressure, longer and more continuous shale smears can be maintained. Shale smears were shown to have a reduction in permeability relative to the original host rock within the initial faulting regime (Takahashi, 2003). This is consistent with porosimetry tests of shale smears by

Eichhubl et al. (2005) relative to their host rock. The reduced permeability of the experimental smears was maintained until they became discontinuous and entrained cataclasites, causing recovered permeability that steadily increased with increasing throw (Takahashi, 2003). Because fault-rock bulk permeability is inversely proportional to capillary entry pressure (Sperrevik et al., 2002), it can be inferred from the experimental regimes of Takahashi (2003) that as shale smears become discontinuous and enter into the fault-rock classification realm of PFFRs, the fault rock will have lower capillary entry pressures as more silt and sand-sized particles are entrained in the fault gouge.

While many fault rock types have been categorized in outcrop and core, a predictive approach needs to be introduced to assess fault-rock type and petrophysical properties in the subsurface prior to CO_2 injection.

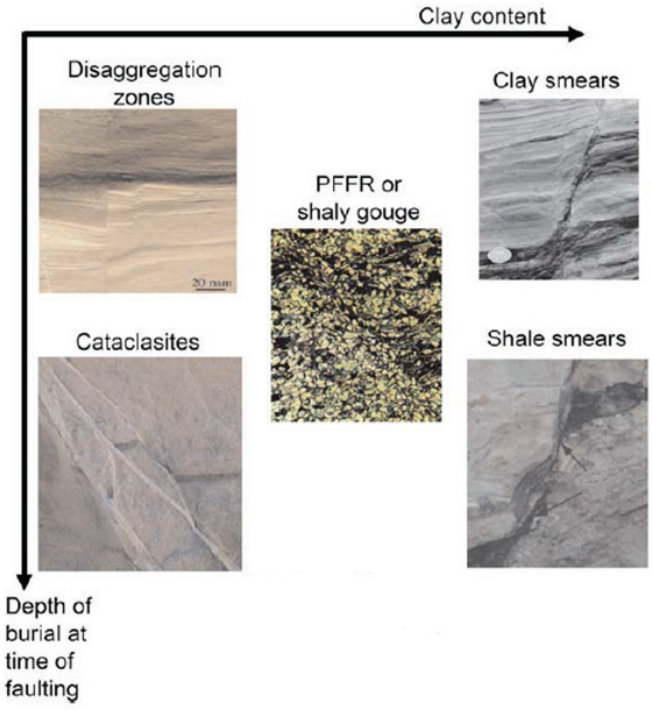

Figure 5. Fault rock types. Modified from Yielding et al. (2010)

Fault Seal Prediction in the Subsurface – the Shale Gouge Ratio

Outcrop and core studies have shown that increasing percent phyllosilicates entrained within the fault gouge increases the capillary entry pressure (Figure 6) and decreases the bulk permeability (Gibson, 1998; Sperrevik et al., 2002; Eichhubl et al., 2005). The capillary entry pressure (discussed in a later chapter), and therefore sealing capacity, shows a linear increase with increasing percent phyllosilicates (termed V_{cl}). This deterministic fault seal approach (Yielding et al., 2010) cannot be accurately applied in the subsurface unless mineralogical analysis of the host rock is available and estimations of the amount of clay entrained in the fault can be calculated. This is difficult to use for predicting fault seal capacity prior to drilling a well.

Previous algorithms for estimating fault rock heterogeneity in the subsurface provided a qualitative assessment using throw and bed thickness, only estimating the ability of a shale bed to form a continuous smear (Bouvier et al., 1989; Lindsay et al., 1993). The more widely accepted Shale Gouge Ratio (SGR) of Yielding et al. (1997) provides a quantitative approach that relies on both fault throw and bed thickness, as well as incorporating the estimated amount of clay within host rock to determine the clay content of fault gouge (Figure 7):

$$SGR = \frac{\sum(V_{cl} * \Delta z)}{throw} \qquad (1)$$

SGR at any point along a fault plane is the summation of the estimate of percent shale in an individual bed (V_{cl}) times the bed thickness (Δz) across the throw

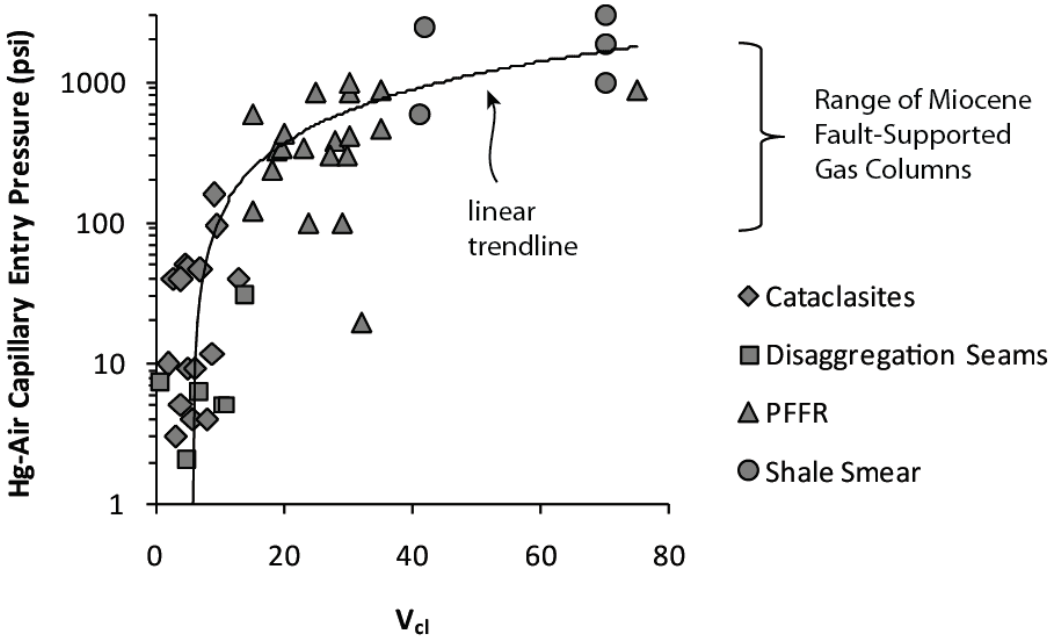

Figure 6. Deterministic fault seal literature review. Data are plotted on a semi-log plot to illustrate the order of magnitude scatter in the cataclasites and phyllosilicate framework rocks (PFFR). Mercury-air (Hg-Air) capillary entry pressure tests are performed perpendicular to the fault plane and the percent phyllosilicates (V_{cl}) in the fault gouge are measured by x-ray diffraction techniques. Data points for fault gouge from normal faults are taken from Gibson (1998), Sperrevik et al. (2002), and Eichhubl et al. (2005).

window, divided by the *throw*, resulting in a unitless estimate of the percent shale in the fault gouge.

The SGR, prior to calibration with subsurface pressure data, has been shown to be an effective qualitative predictor for sealing versus non-sealing faults (Figure 8) (Yielding, 2002). SGR data from the fault bounded reservoirs of both sealing and non sealing faults show that SGR values of approximately 15-20% are the cutoff for sealing versus nonsealing faults.

However, to approach quantitative fault seal predictions in the subsurface, estimates of SGR must be calibrated to natural accumulations of oil and gas and their associated fluid properties. Before calibrating fluid properties to fault rock properties, it's important to understand what governs the membrane sealing capacity of fault rock.

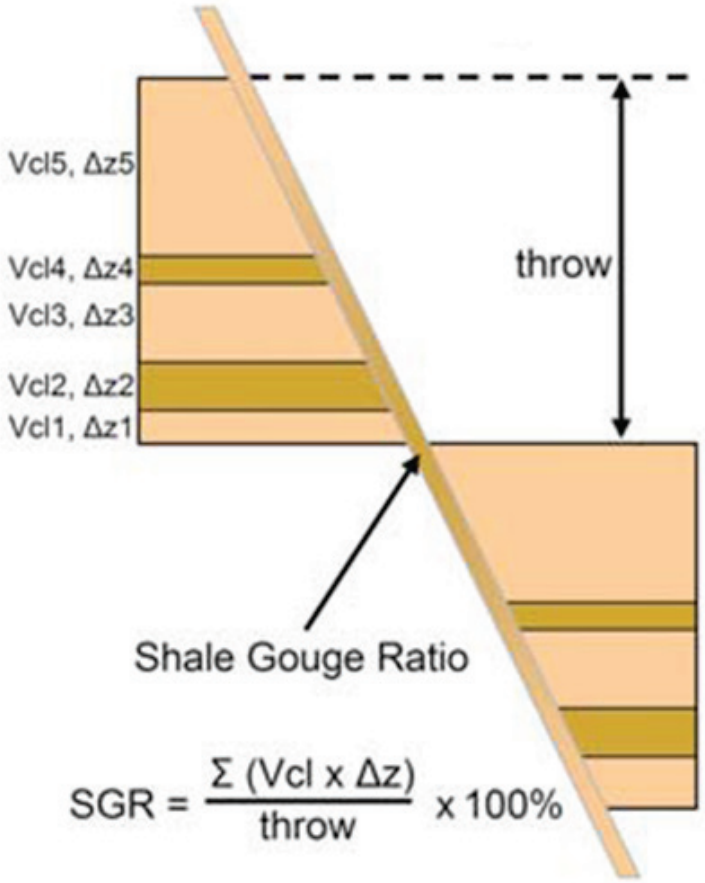

Figure 7. Shale gouge ratio (SGR). Modified from Yielding et al. (2010).

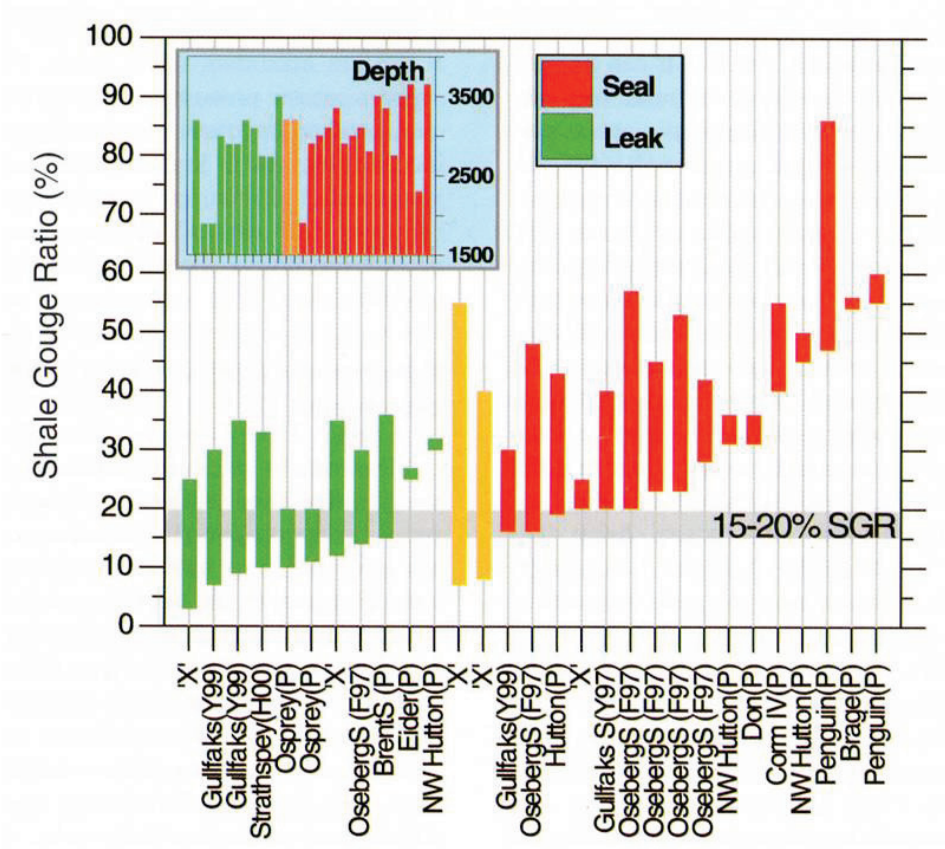

Figure 8. Qualitative use of the SGR. SGR shows sealing vs leaking faults from various North Sea fields. Image from Yielding (2002).

Buoyancy Pressure and Capillary Entry Pressure

Fluids of interest for fault seal calibration, such as methane, oil, and CO_2, are less dense than brine and therefore migrate vertically and laterally through rocks, exerting a buoyant force. Buoyancy pressure is the force exerted by the density contrast between the wetting phase and the non-wetting phase, in this case assumed to be either brine-CO_2 or brine-methane:

$$P_b = (\rho_w - \rho_f) * 0.433 * H \quad , \qquad (2)$$

where P_b is the buoyancy pressure (psi), ρ_w is brine density (g/cm^3), ρ_f is the density of the buoyant fluid (g/cm^3), and H is total column height (ft) (Schowalter, 1979). Buoyancy pressure increases by increasing column height, decreasing depth within a fixed column height, or increasing wetting (water) and non-wetting phase density contrast (Figure 9). The confining geologic units that trap the buoyant fluid (i.e. top seal and fault seal) restrict fluid movement due to the capillary forces associated with the smaller pore throat radii typical in seals. The capillary entry pressure for the fault-rock or top seal with cylindrical pore throats is governed by a variation of the Laplace law:

$$P_{ce} = \frac{2\sigma cos(\theta)}{r} * 0.145 \quad , \qquad (3)$$

where P_{ce} is the capillary entry pressure (psi), σ is interfacial tension (mN/m) between the wetting and non-wetting phase, θ is the wettability (degrees), expressed as the contact angle between the wetting and non-wetting phase and the solid pore throat, and r is mean interconnected pore throat radius (μm) (Purcell, 1949; Schowalter, 1979) (Figure 10). For static, trapped methane fields from the Lower Miocene in the Gulf Coast under near-

hydrostatic conditions, it is assumed that the buoyancy pressure (P_b) exerted by the trapped methane column equals the limiting seals capillary entry pressure (P_{ce}):

$$P_b = P_{ce} \quad (4)$$

This is only the case if the rate of charge does not exceed the rate of leakage by capillary flow and the methane column is not limited by structural spill, juxtaposition spill, mechanical top seal failure, or fault reactivation. If the methane column is limited by any of the spill or failure mechanisms, then the buoyancy pressure of that methane column represents a minimum estimate of the fault seal or top seal capillary entry pressure.

Buoyancy pressures exerted from different fluid column heights at varying reservoir depths (varying temperatures and pressures) require normalization. Fluid properties affecting buoyancy pressure and capillary entry pressure, such as fluid density, interfacial tension, and contact angle, have been shown to vary for the same fluid type depending on temperature, pressure, and brine salinity (Firoozabadi and Ramey, 1988; Argaud, 1993; Chalbaud et al., 2006; Chiquet et al., 2007b).

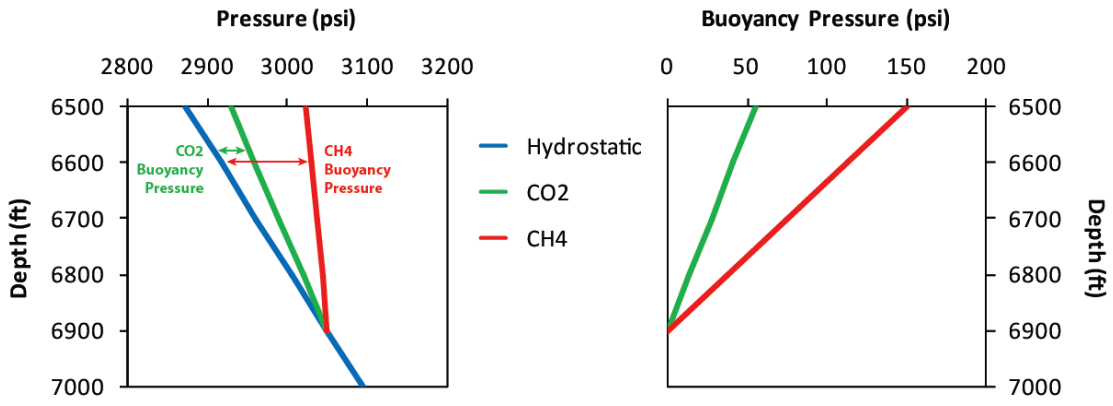

Figure 9. Hypothetical buoyancy pressure. Hypothetical pressure vs depth profile (left) illustrating the different pressure trajectories due to buoyancy for CO_2 (ρ = 0.7 g/cm^3), and CH4 (ρ = 0.15 g/cm^3). Brine density is 1.05 g/cm^3. Buoyancy pressure versus depth (right) for the same pressure profile.

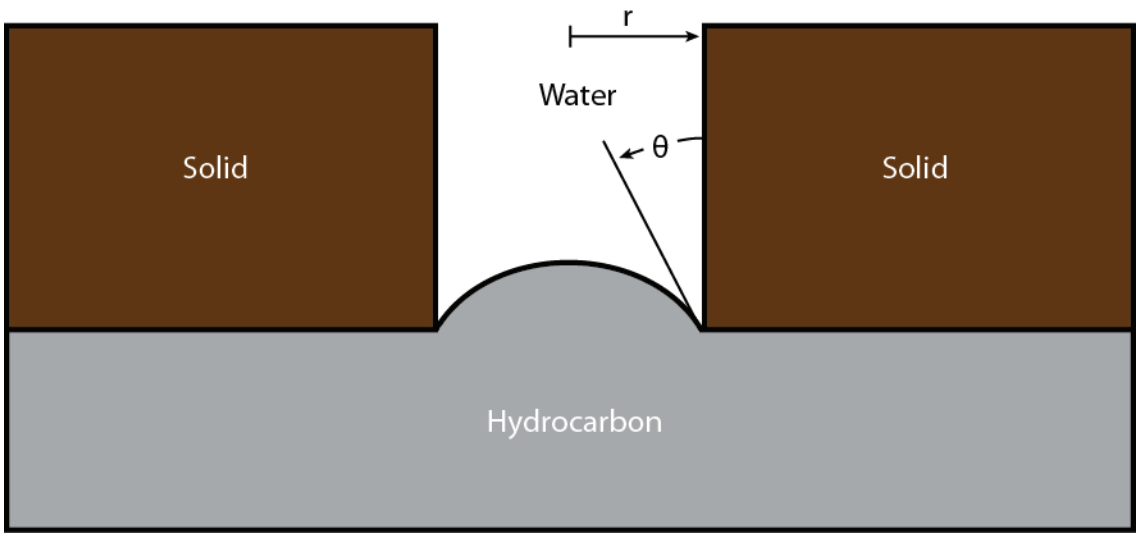

Figure 10. Capillary entry schematic. The hydrocarbon (non-wetting) and water (wetting) form a contact angle (θ) with the solid substrate. Pore throat radius is represented as 'r.' Image modified after Schowalter (1979).

Fluid Properties and Their Effect On Capillary Entry Pressure

Column heights composed of the same fluid (e.g. methane) that are representing the capillary entry pressure of the fault gouge or top seal must be normalized if their buoyancy pressures are measured at varying depths in the subsurface (varying temperatures and pressures). Therefore, an understanding of modeled fluid properties based on regional temperature, pressure and salinity trends is necessary for predicting the sealing capacity of faults and top seals.

TEMPERATURE & PRESSURE

Regional temperature and pressure data have been compiled from wells and produced fields within the Miocene section of the Texas State Waters. Ninety three temperature measurements from well logs and 198 average reservoir temperature measurements (Seni et al., 1997) show an approximately 23°C/km gradient within the Miocene section (Figure 11A). Temperature gradients begin to increase around 14,000ft where some wells penetrate the Anahuac shale on the footwall of the Clemente-Tomas fault system. Average temperature can be expressed by the equation:

$$T = 0.602D^2 + 4.158D + 98.49 \quad , \qquad (5)$$

where T is temperature (°F) and D is depth (kilofeet). This temperature trend is consistent with findings from nearby offshore geothermal studies (Nagihara, 2010).

Average initial reservoir pressure (Seni et al., 1997) trends for all Miocene reservoirs within the State Waters are shown to be hydrostatic until depths of approximately 9,000ft. This depth is geographically variable and should only be used as

a rule of thumb. The overburden stress, or S_v for normal-fault stress regimes, is assumed to be an average of 1 psi/ft. In the absence of conventional stress magnitude measurements, such as leakoff tests (Hickman and Zoback, 1983), the overpressured reservoirs provide a reasonable estimate for the minimum principal stress magnitude of 85% S_v. These values are consistent with the findings of Engelder and Leftwich Jr. (1997).

FLUID DENSITY

The average temperature trend with depth and hydrostatic pressure gradient were input into the Peng-Robinson equation of state to solve for CO_2 fluid density with depth (Peng and Robinson, 1976). The program ThermoSolver™ was used to automate the Peng-Robinson equation of state (Barnes and Koretsky, 2003) resulting in average density trends with depth for both CO_2 and methane (Figure 11C). CO_2 density rapidly increases with depth until it reaches a steady range between 0.6 and 0.7 g/cm^3 below 1km depth. Maximizing CO_2 density can greatly increase storage capacity and should be considered when choosing a sequestration site. Calculated CO_2 density at field-specific measured Miocene reservoir temperature and pressures (Seni et al., 1997) show that when overpressure is taken into account, as opposed to hydrostatic pressure, CO_2 density can approach 0.9 g/cm^3 (grey dots, Figure 11C).

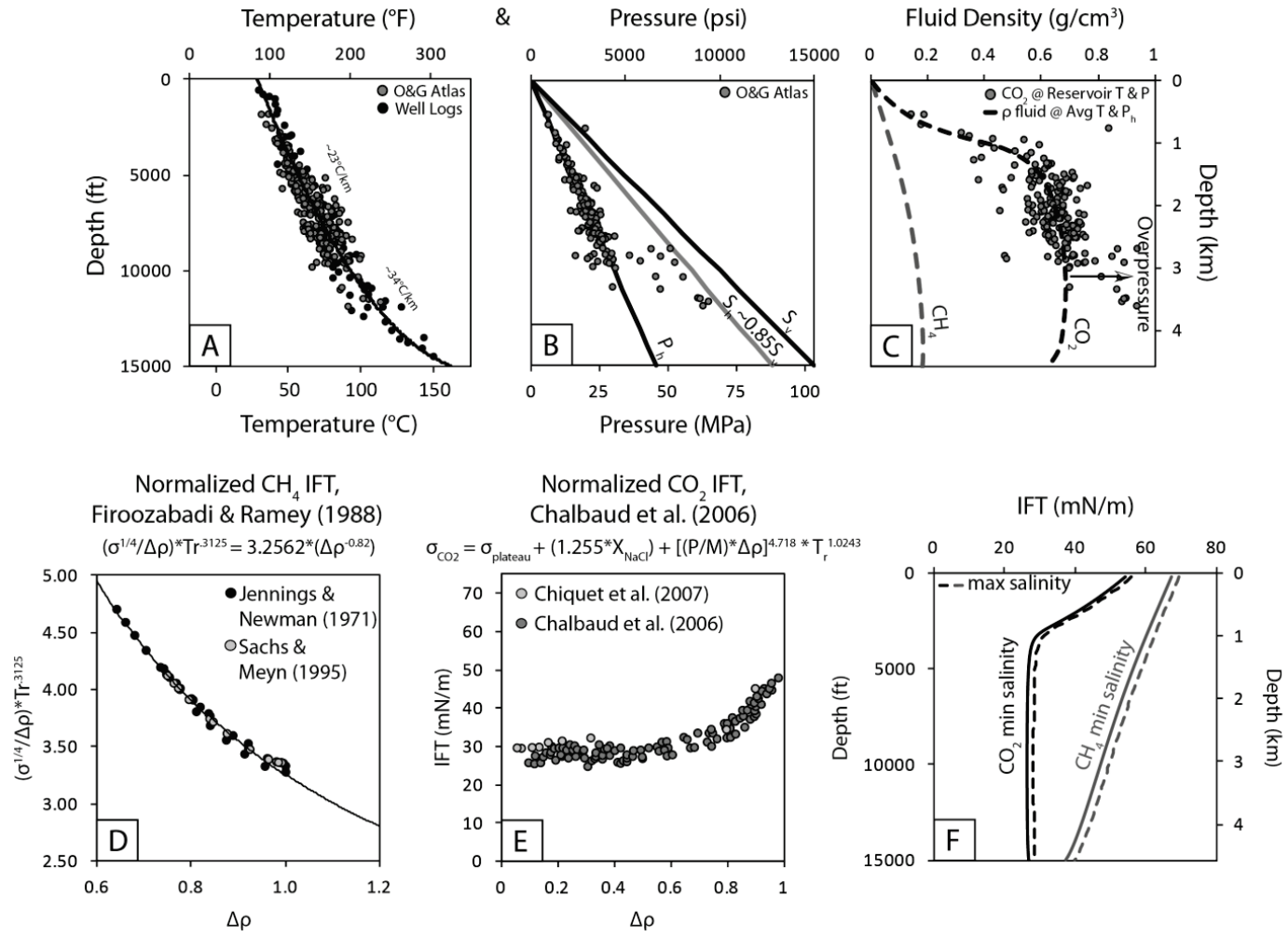

Figure 11. Temperature, pressure, density, and interfacial tension trends with depth.

Buoyancy pressure and fluid gradients are normally obtained from in-situ measurement of reservoir pressures at varying depth increments. These measurements are used to demonstrate reservoir connectivity (or lack thereof). In the absence of such data, the temperature and initial reservoir pressure can be used to calculate a fluid density using the Peng-Robinson equation of state. This is only effective for pure fluids such as methane and CO_2. The calculated methane density and known, mapped column heights can then used to calculate buoyancy pressure (Equation 2).

INTERFACIAL TENSION

The interfacial tension (or attraction) between two immiscible fluids is a key parameter in Equation (3). The higher the interfacial tension between two fluids, the more attracted they are and the more pressure is required to displace the wetting fluid. In other words, higher interfacial tension yields a higher sealing capacity (when all other external factors are constant). Macleod (1923) used the Van der Waals' equation assumption that force of attraction falls off with the 4th power of the distance between molecules. He found that the surface tension of a liquid and its vapor is dependent upon the empirical formula:

$$C = \frac{\sigma}{(\rho_l - \rho_v)^4} \quad , \qquad (6)$$

where C is a constant, σ is the surface tension of a pure compound, and ρ_l and ρ_v are the liquid and vapor densities, respectively. Surface tension is directly proportional to the density difference between the two fluids. Therefore, as the density difference decreases, the interfacial tension between two immiscible fluids decreases.

Experimental findings on methane-brine interfacial tensions (Hough et al., 1951; Jennings and Newman, 1971) were analyzed by Firoozabadi and Ramey (1988) and, using Equation (6) for an initial evaluation, interfacial tension (IFT) was shown to vary with both density contrast ($\Delta\rho$) as well as reduced temperature (T_r). Reduced temperature is a dimensionless scaling factor:

$$T_r = \frac{T}{T_c} \ , \qquad (7)$$

where T is the measured temperature of the gas or supercritical fluid and T_c is the critical temperature at which point a fluid becomes supercritical (Peng and Robinson, 1976). T_c for CH_4 and CO_2 are 190.15K and 304.15K, respectively (Atkins and Jones, 2005). Using the relationships between $\Delta\rho$ and T_r established Firoozabadi and Ramey (1988), as well as the interfacial tension measurements from Jennings and Newman (1971) and Sachs and Meyn (1995), the following equation for pure water-methane interfacial tension was fit to the data in Figure 11D:

$$\frac{\sigma^{0.25}}{\Delta\rho} T_r^{0.3125} = 3.2562 * \Delta\rho^{-0.82} \qquad (8)$$

Therefore, given the density contrast between the wetting and non-wetting phase of a reservoir, and the temperature of the reservoir, the interfacial tension of methane-brine can be calculated at depth using the temperature and pressure trends.

Brine-CO_2 interfacial tensions cannot be estimated using $\Delta\rho$ and T_r alone. The effects of CO_2 solubility and, to a lesser extent, salinity must be taken into account (Chalbaud et al., 2006; Chiquet et al., 2007b) (Figure 11E). IFT experiments consider varying reservoir temperatures, pressures, and salinities, and therefore varying CO_2

densities and CO_2-saturated brine densities. The empirical equation from Chalbaud et al. (2006) to predict CO_2-brine IFT is:

$$\sigma_{CO2} = \sigma_{plateau} + (1.255X_{NaCl}) + [(\frac{P}{M}) * \Delta\rho]^{4.718} * T_r{}^{1.0243} \quad , \qquad (9)$$

where $\sigma_{plateau}$ is 26 mN/m; X_{NaCl} is the NaCl molality equivalent of the target brine reservoir; P, the parachor number, is a scaling constant of 82; M is molar mass equal to 44.01 g/mol; $\Delta\rho$ is the density difference between the CO_2-saturated brine and the CO_2; and T_r is the reduced temperature. Salinity is taken into consideration within Equation (9) for CO_2, but not in Equation (8) for methane. Adding the effect of salinity for methane is discussed in a subsequent section.

Both methane and CO_2 density increase with depth (increasing temperature & pressure) and therefore the density difference between brine (nearly incompressible) and the buoyant fluid decreases. As the density difference decreases, the interfacial tension should decrease (Equation 6). Therefore, both methane-brine and CO_2-brine interfacial tensions decrease with depth as expected (Figure 11).

Using the average temperature and pressure curves (Figure 11), it should be noted that the error caused by CO_2 solubility on the $\Delta\rho$ calculation will never be more than 5% (Figure 12). Still, it is something to take into consideration for settings with extremely saline brines.

SALINITY

The CO_2 IFT experiments of Chalbaud et al. (2006) showed that with increases in brine molality (XNaCl), the CO_2-brine IFT also increased. Since the Firoozabadi and

Ramey (1988) correlation uses experiments that were done on CH4-pure water IFT, an inquiry into the error owing to salinity on CH4-brine IFT calculations is warranted. The free cations at the water interface with CH_4 will increase the ratio of charge to cation surface area that the water 'feels' and thus increases the surface tension (Argaud, 1993).

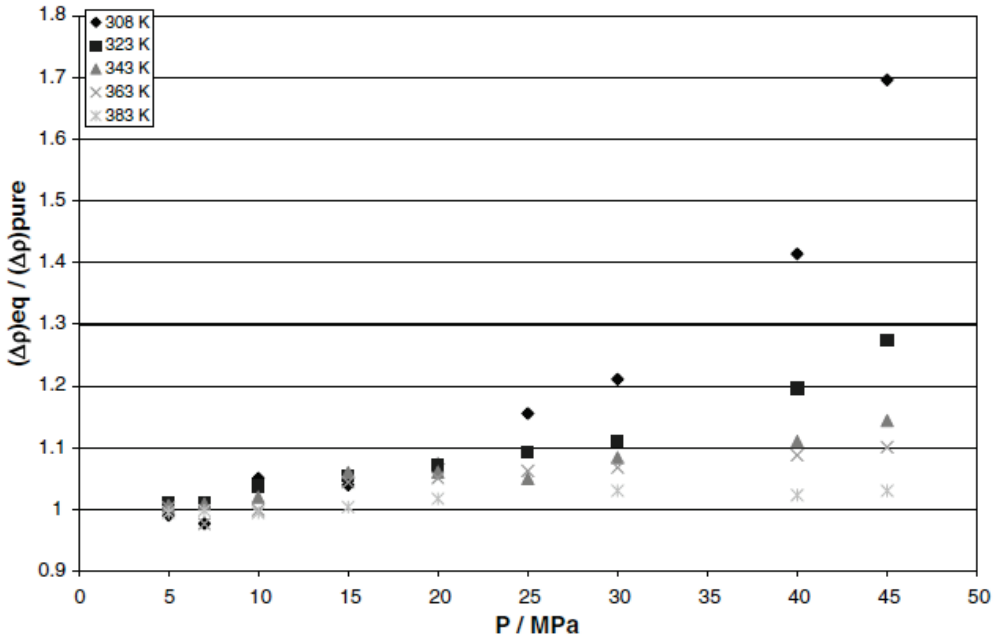

Figure 12. Ratio of CO_2-brine density in equilibrium and pure CO_2 density (y-axis) vs. pressure (x-axis) for varying reservoir scale temperatures. Image from Chiquet et al. (2007b).

Argaud (1993) found the relationship between cation molality and IFT increase to be linear for a range of molalities. The simple linear function for X_{NaCl} is:

$$\delta\sigma = 1.63X_{NaCl} \ , \qquad (10)$$

where the increase in IFT ($\delta\sigma$) is 1.63 mN/m per molal NaCl (X_{NaCl}). Maximum NaCl molality from the USGS Produced Waters Database (Breit, 2006) for Gulf Coast Miocene brines in Texas is 1.63m (Appendix B). Samples from the database for this region have a maximum depth of about 8,200ft. Using 1.63m as the maximum X_{NaCl} (Equations 8, 9 & 10), it can be seen that variations in salinity have a minor effect of up to a few units of IFT (Figure 11F).

CONTACT ANGLE

Contact angle between brine and the non-wetting fluid can vary with non-wetting fluid type, pressure, salinity, and mineralogy of the seal (Chiquet et al., 2007a; Espinoza and Santamarina, 2010). Experimental contact angle studies between supercritical CO_2 and brine have been compared with theoretical calculations (Meckel, 2010) to determine that a θ of 30° should be used for modeling. In this paper, contact angle will remain at 0° (considered optimistic) for both CO_2-brine and CH_4-brine, but it should be noted that changing θ from 0° to 30° for CO_2-brine will yield a smaller $\cos(\theta)$, from 1 to 0.866, respectively (i.e. a 13.4% reduction in sealing capacity).

MERCURY-AIR NORMALIZATION

If the buoyancy pressure of a methane column acting on a fault is considered to reflect the capillary entry pressure of the fault, then the capillary entry pressure must be converted to mercury-air capillary entry pressure before it can be compared with similar or different fluids at varying depths (i.e. different interfacial tensions).

Fluids have different capillary entry pressures for the same pore throat diameter based on their varying interfacial tensions (Equation 2). Buoyancy pressures from different Miocene methane-brine columns must be normalized to a common standard, such as mercury-air, in order to compare the sealing capacity of different fault-rock and top seal over varying depths:

$$P_{chw} = \frac{\sigma_{hw} * \cos(\theta_{hw})}{\sigma_{ma} * \cos(\theta_{ma})} P_{cma} \quad (11)$$

where P_{chw} is the hydrocarbon-water capillary entry pressure, P_{cma} is mercury-air capillary entry pressure, σ_{hw} is the hydrocarbon-water interfacial tension, σ_{ma} is the mercury-air interfacial tension (480 dyne/cm), θ_{hw} is the hydrocarbon-water contact angle (usually considered to be 0° in water-wet rocks), and θ_{ma} is the mercury-air contact angle (40°) (Schowalter, 1979).

Calibrating the Quantitative Fault Seal Failure Envelope

Having established the fluid properties and theory behind the capillary entry of varying fault gouge, the estimations of clay content in fault gouge calculated by the shale gauge ratio (SGR) must first be calibrated to field data in order to ultimately calculate and compare membrane fault seal and fill-to-spill CO_2 capacity estimates. Quantitative fault seal analysis using various algorithms, especially the SGR, have been most readily applied in the Gulf of Mexico (Alexander and Handschy, 1998; Davies et al., 2003; Kim et al., 2003), the North Sea (Freeman et al., 1998; Ottesen Ellevset et al., 1998; Harris et al., 2002; Childs et al., 2002; Færseth et al., 2007; Bretan et al., 2011), the Otway Basin (Lyon et al., 2005), the North West shelf of Australia (Jones and Hillis, 2003), and the Niger Delta (Bouvier et al., 1989; Jev et al., 1993).

THE GLOBAL FAULT SEAL DATABASE

Global comparisons of fault seal have been developed over the last two decades (Figure 13) (Yielding, 2002; Bretan et al., 2003; Yielding et al., 2010). The global fault seal data points were determined from over 10 fault bound reservoirs (Graham Yielding, Badleys Geoscience, personal communication, 2012) using field data (V_{sh} logs, structural models, fluid contacts, and pressure gradients). For a given value of SGR (calculated) along a fault there is an associated buoyancy pressure (extrapolated from measured pressure data) acting on the same point of the fault within the hydrocarbon reservoir interval. This provides many data points for a single fault bound trap, but only one true weak point, or the highest ratio of buoyancy pressure and SGR. The dashed lines

represent the fault seal failure envelopes bounding the weak point values. Most importantly, the fault seal failure envelopes represent a quantitative calibration of the maximum amount of buoyancy pressure for a particular fluid that a given value of SGR can seal (Bretan et al., 2003). The fault seal failure envelope equations (linear, similar to the deterministic data presented in Figure 6) allow for the prediction of maximum buoyancy pressure, and therefore maximum column height, that an untested fault block could sustain. The different colored dashed lines represent a given reservoir depth interval as defined by the author (blue: <3.0km, red: 3.0-3.5km, and green >3.5km). Equations for the less than 3km and greater than 3.5km depth lines are given, respectively,

$$(<3.0\text{km})\ BP = 0.175 * SGR - 3.5 \qquad (12)$$

$$(>3.5\text{km})\ BP = 0.150 * SGR + 1.9\ , \qquad (13)$$

where the maximum *BP* (buoyancy pressure, bars) that a fault segment with a given *SGR* is able to withstand is a linear fit and increases with increasing SGR (Yielding et al., 2010). These equations are then converted to PSI (1bar = 14.503psi):

$$(<3.0\text{km})\ BP = 2.538 * SGR\ -\ 50.76 \qquad (14)$$

$$(>3.5\text{km})\ BP = 2.175 * SGR\ +\ 27.55\ , \qquad (15)$$

and normalized to mercury-air capillary entry pressure so that fluids from different depths can be compared. This is not explicitly shown by Yielding et al. (2010) since there is no mention as to what fluid types (oil, gas, or both) were used for their global calibration. However, it is stated that a 10x multiplier can be applied to normalize the published

equations to mercury-air (Yielding et al., 2010) based on Equation (11), and yields the following equations:

$$(<3.0\text{km})\ BP_{ma} = 25.38 * SGR\ -\ 507.6 \qquad (16)$$

$$(>3.5\text{km})\ BP_{ma} = 21.75 * SGR\ +\ 275.5\ , \qquad (17)$$

where BP_{ma} is the mercury-air equivalent buoyancy pressure, or maximum sealing capillary entry pressure according to Equation (4). Equations (16) and (17) from the global dataset will be compared to the calibration from the local Miocene data.

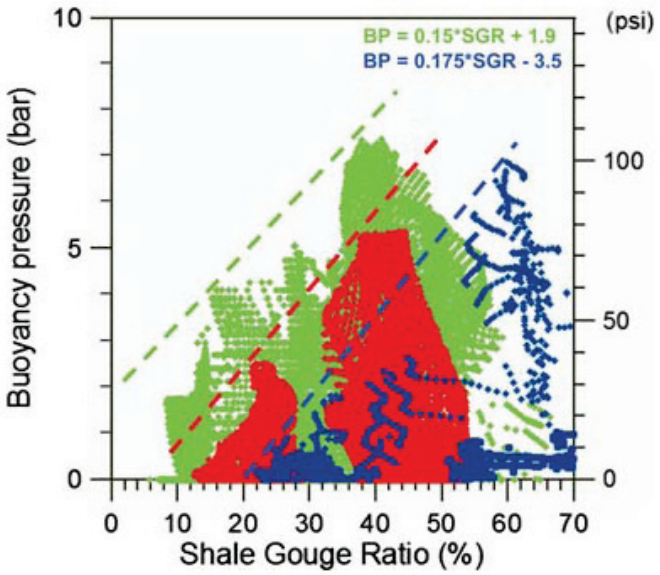

Figure 13. Global fault seal calibration database. Dashed lines represent fault seal failure envelopes. Colors represent depths of sealing faults: blue (< 3km), red (3 - 3.5km), and green (>3.5km). Image from Yielding et al., (2010).

Depth relationships to membrane fault seal capacity, as presented by the Yielding et al. (2010) fault seal failure envelopes, are variable, depending on fluid properties

(Firoozabadi and Ramey, 1988; Chalbaud et al., 2006), across fault pressure differences (Underschultz, 2007), and depth (effective stresses) at time of faulting (Sperrevik et al., 2002; Takahashi, 2003). Owing to this variability it is suggested that the SGR always be calibrated to the basin, and more specifically, the target reservoirs of interest.

FAULT SEAL CALIBRATION WORKFLOW FOR HISTORIC NATURAL GAS FIELDS

SGR is normally calculated using field scale, 3D-seismic-derived structural models of fault & stratigraphic data in conjunction with pressure data from wells within different fault blocks. This application is time consuming and normally utilized over many years of exploration and development with contributions from many disciplines. In an effort to reduce the duration of these analyses and still effectively calibrate a fault seal failure envelope for a desired basin, an older methodology (with established concepts) is applied to historic field publications for the results shown below. SGR can still be calculated as long as structure maps exist with fluid contacts (for calculating column height and fault throw) and original reservoir pressure & temperature data exist (for calculating methane density). An atlas of field maps and reservoir properties is available for fields in the Texas State Waters (Seni et al., 1997). One-dimensional triangle diagrams can be used to calculate SGR as it varies along a fault with known offsets (Knipe, 1997; Childs et al., 2002) by using a base stratigraphic column from an unfaulted gamma ray (GR) log converted to volume shale (V_{sh}). Converting GR to V_{sh} gives a reliable estimate of the amount of clay within the stratigraphy:

$$V_{sh} = \frac{GR - GR_{min}}{GR_{max} - GR_{min}} , \qquad (18)$$

where *GR* is the measured GR, GR_{min} is the average GR response of clean sandstones, and GR_{max} is the average GR response of shale (Bhuyan and Passey, 1994). It is recommended that the 10th percentile GR value be used for GR_{min} and the 90th percentile GR value be used for GR_{max} for stratigraphic intervals spanning thousands of feet. The Brazos Block 440 Field B-sand (Figure 14) (Lane and Pace, 1998) is one of four fields evaluated for SGR calibration. Two of the gas columns (northern and southern fault block) within the field are evaluated.

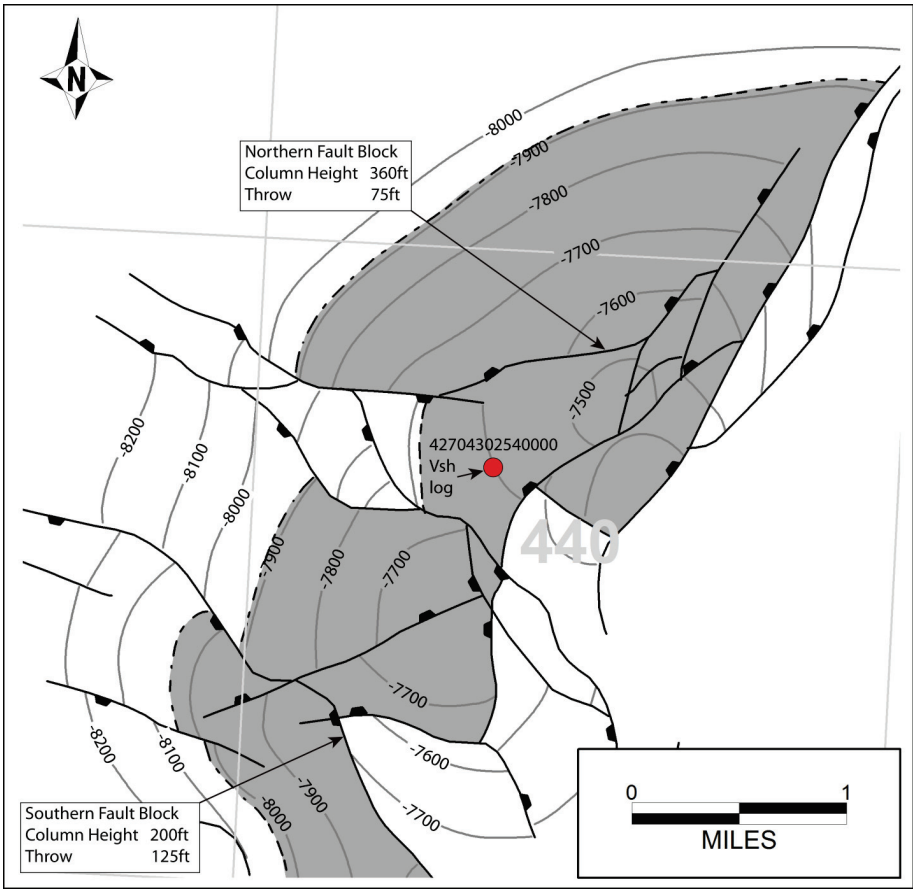

Figure 14. Structure map of the Brazos Block 440 B sand. Modified from Seni et al. (1997)

Methane density is calculated from Peng and Robinson (1976) using the average reservoir temperature and pressure. Methane density and column height are then applied to Equation (2) to calculate the buoyancy pressure exerted by the methane column at the crest of the structure, a better assumption weak-leak point test than across-fault differential pressure (Fisher et al., 2001). The buoyancy pressure is then converted to mercury-air equivalent pressure (Equation 11) which plots on the Y-axis of the fault-seal failure plot (Figure 13).

V_{sh} is then calculated for the unfaulted, representative stratigraphic section using a GR log. V_{sh} is evaluated using a standard triangle diagram (Figure 15 for the Brazos Block 440 B-sand) to calculate SGR (Equation 1) at the crest of the structure (maximum column height). Four other methane columns from fields within the Texas State Waters were evaluated (Appendix C) using this workflow (Figure 16A).

CALIBRATION RESULTS

Fault-bounded methane columns at reservoir depths less than 3.0km depth (blue triangles, Figure 16A, left) correlate to the global fault-seal failure envelope of Yielding et al. (2010). This correlation shows that for the Miocene section in the Texas State Waters, the less than 3.0km fault seal failure envelope (Equation 16) can be used to estimate membrane fault seal capacity. The single fault bounded methane column from a depth greater than 3.0km (green triangle, Figure 16A, left) corresponds to a reservoir depth between 3.0-3.5km, and incidentally it falls in the middle of the ≤3.0km line and >3.5km line of Yielding et al. (2010), showing an increase in sealing capacity for the

same SGR with increasing depth. Fault-bounded methane column heights for 11 reservoirs ≤3.0km and 10 reservoirs >3.0km (Figure 16A, right) either lack detailed across-fault mapping or a GR log for calculation of SGR. All column height data are listed in Appendix D. A general increase in column height gives justification to the increase of sealing capacity of faults with depth.

Top seal capacity is necessary to incorporate into robust capacity estimation models (Divko et al., 2010), however, fault seal is often ignored while preference is given to top seal investigations. Top seal values (10% MICP) from 6 LM1 mudstone and siltstone mercury-injection capillary pressure (MICP) tested lab samples (10,578-10,604' depth, or 3.225-3.233 km, well OCS-G-4708#1) are shown on the rightmost vertical axis of Figure 16A (Jiemin Lu, Bureau of Economic Geology, personal communication, 2011). The lowest two top seal values are from siltstone samples (1103 psi and 1200 psi) and are still more effective seals than most of the ≤3.0km fault seals. This shows that natural accumulations of methane in fault bounded traps are critically limited by the sealing capacity of faults, not top seal capacity.

However, top seal capacity can be a limiting factor, no matter how large the fault sealing capacity is (Figure 16B). Indeed, one of the methane columns appears to be limited by top seal (Middle Bank Reef 6000' reservoir, SGR=64, BP_{ma}=510 psi, Appendix C). Five of the six methane columns analyzed correlate with published fault seal failure envelopes and are interpreted to be fault seal limited (Figure 16C).

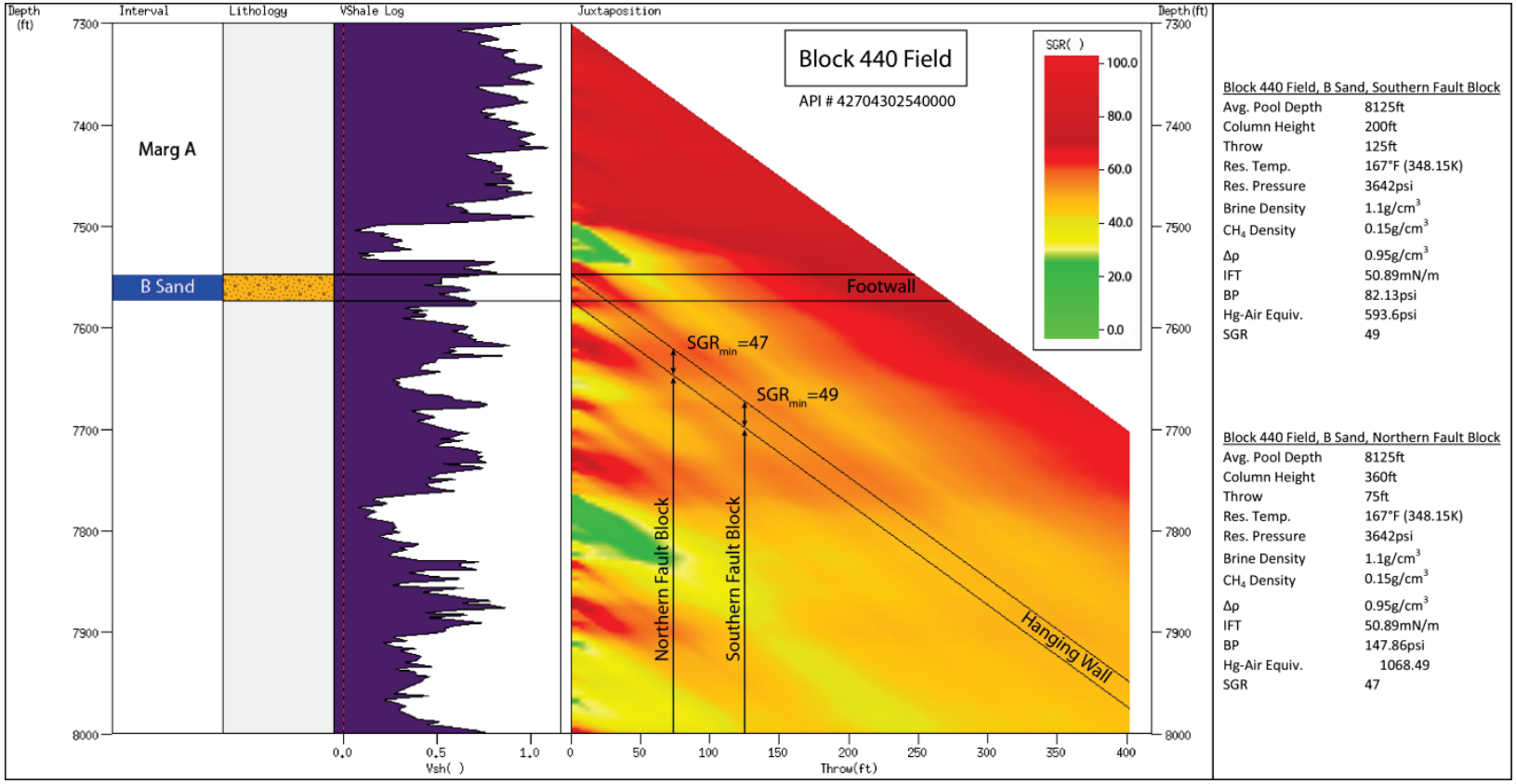

Figure 15. Triangle diagram for the Brazos Block 440 B sand.

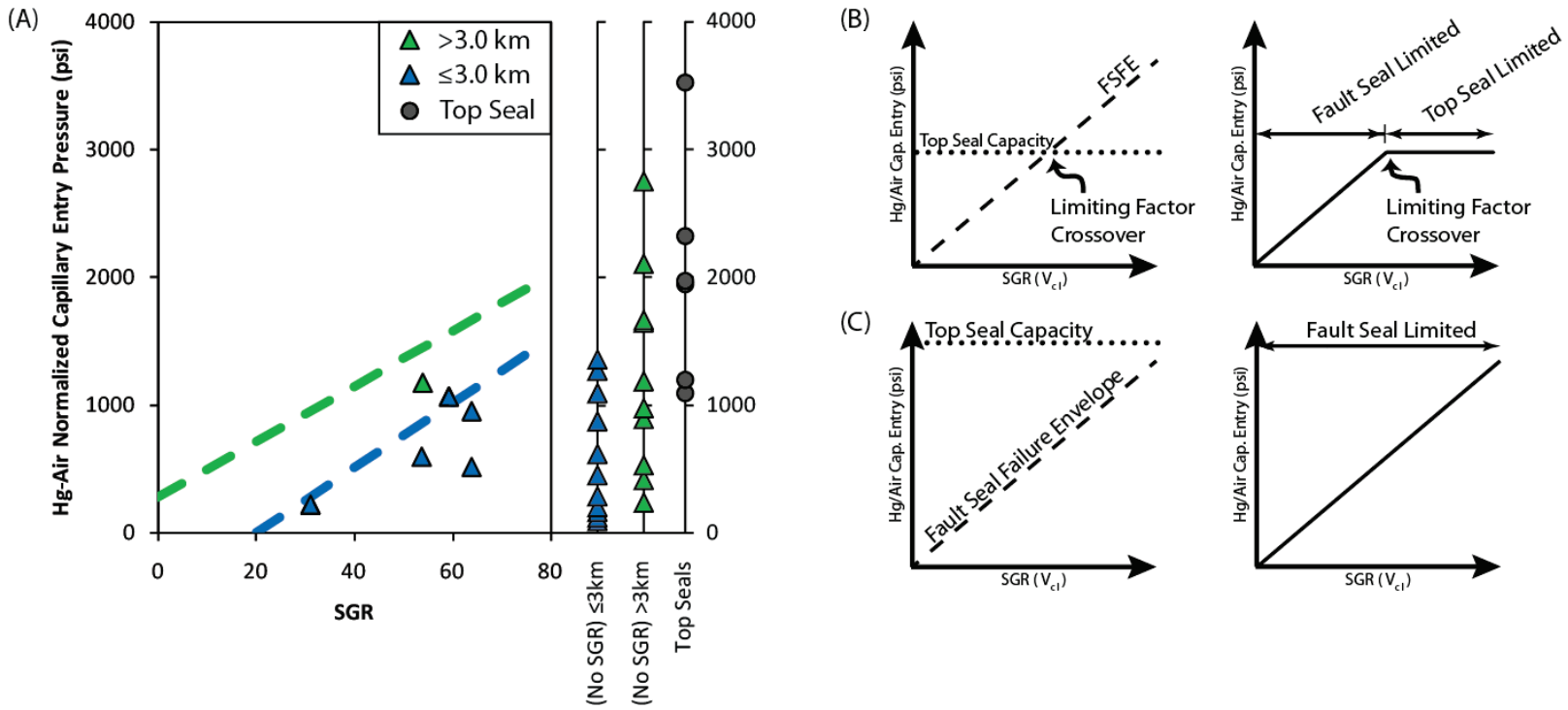

Figure 16. Calibrated Lower Miocene fault seal & top seal. (A) Calibrated fault seal failure envelope. The blue dashed line and green dashed line correspond to Equations (16) and (17), respectively, from the global fault seal database. Blue and green triangles correspond to data points ≤3.0km and >3.0km, respectively. Column heights lacking SGR calculations are displayed on two vertical axes (≤3.0km & >3.0km). Top seal mercury injection capillary pressure data are plotted on the rightmost vertical axis. (B) Schematic diagram in which top seal capacity limits the fault bound column height. (C) Schematic diagram similar to (A), where the fault seal is the dominant limiting factor on sealing capacity.

Shale smears can have a higher sealing capacity than the host-rock shale it was derived from owing to shearing (Takahashi, 2003; Eichhubl et al., 2005). However, empirical subsurface field observations (Figure 16A) show that the column heights sealed are lower than the stratigraphically equivalent top seal. Since shale smears increase the sealing capacity of fault rock relative to their host rock (Eichhubl et al., 2005), the faults would likely have an average sealing potential equivalent to the average top seal values if they were smears. Since they are lower than the equivalent top seals, and fall in the range of deterministic PFFR seal capacity (Figure 6), these calibrated data suggest that PFFRs, not shale smears, are the dominant sealing fault rock type.

FAULT SEAL VARIATION WITH DEPTH

Global depth relationships for fault seal capacity have shown a general increase with depth (Sperrevik et al., 2002; Yielding et al., 2010), but the preliminary sorting of Gulf of Mexico Miocene data (Figure 16) show a disagreement with using discrete depth cutoffs (e.g. >3.0 km values). The 27 aforementioned fault-bound methane column heights and buoyancy pressures were sorted based on the average pool depth of the reservoir (Figure 17). Methane IFT for each specific reservoir temperature, pressure, and methane density was calculated (Equation 8) and then each buoyancy pressure was converted to mercury-air equivalent pressure (Equation 11 with a contact angle of 0°) (Figure 17 and Appendix D). These data (depth versus column height) show a trend of increasing fault-seal capacity with depth.

Column height data must be considered in the context of the percent overpressure (Figure 17) of the reservoir in question due to potential across-fault pressure sealing capacity support (Brown, 2003):

$$\%\ Overpressure = \left(\frac{IP - P_{hydro.\ equiv}}{S_{v\ equiv} - P_{hydro.\ equiv}}\right) x\ 100\ , \qquad (19)$$

where *IP* (psi) is the initial reported reservoir pressure, $P_{hydro.\ equiv}$ (psi) is the hydrostatic equivalent pressure of the average reservoir depth (0.445 psi/ft), and $S_{v\ equiv}$ is the estimated overburden pressure at the average reservoir depth (1.0 psi/ft). Without detailed pressure data from the field it is impossible to tell if the increasing column heights with depth are the result of across-fault pressure support, or hydrodynamic seal (Schowalter, 1979; Watts, 1987; Losh et al., 1999; Davies et al., 2003; Brown, 2003; Underschultz, 2007). The increasing fault seal capacity can be attributed more accurately to increased mechanical compaction and cementation (Lander and Walderhaug, 1999) with depth, as well as potentially increased depth (or more accurately, increased effective stress) at time of faulting (Sperrevik et al., 2002; Takahashi, 2003).

While the depth trend for fault seal may potentially be a problem at great depths, economic sequestration of CO_2 will likely target shallow reservoirs (i.e. <3km) and therefore the fault seal calibration (Equation 16) can be used to model fault bound traps for CO_2 sequestration within the Lower Miocene of the Texas State Waters. Further investigations of depth relationships on fault seal capacity are not delineated.

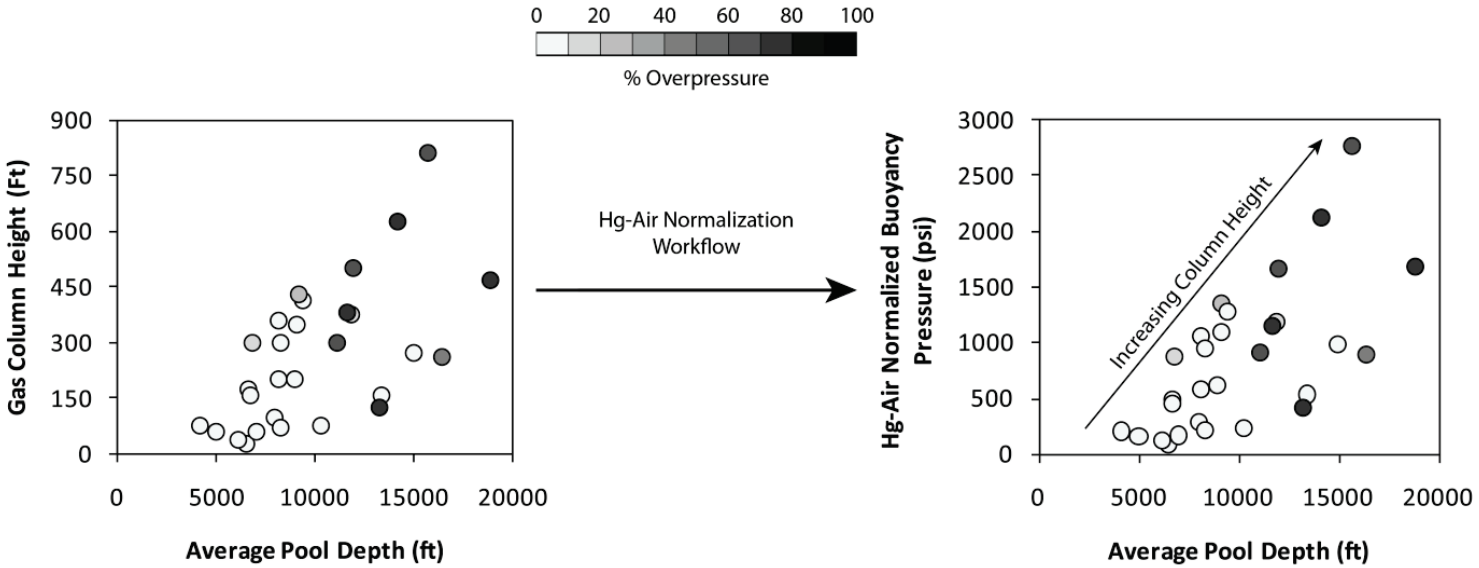

Figure 17. Fault bound column heights trends with depth. 27 fault supported column heights (left) converted to mercury-air equivalent buoyancy pressures (right). Data points are shaded by % overpressure.

Modeling Membrane Fault Seal for a Potential Sequestration Prospect

Potential CO_2 sequestration prospects (Figure 3A) highlight the need for membrane fault seal modeling in order to assess site specific CO_2 capacity. The piercement salt diapir adjacent to San Luis Pass, Galveston (Figure 1) has been chosen for modeling due to its proximity to anthropogenic CO_2 sources. The southeast fault block of the LM2 horizon (Figure 18) has been chosen as the potential sequestration target due to its potential ability to structurally contain migrating fluids, lack of near-surface penetrating faults, a thick (>500ft) Amph. B. top seal, and an average reservoir depth (7,500ft) for maintaining dense, supercritical CO_2. The southeast fault block is bound on the west by the A Fault and to the north by the B Fault (Figure 18). The average dip of 16° on the structure allows for some certainty that the fluids would migrate toward the NW to the top of the structure. The LM2 horizon (Figure 19, also used for V_{sh} calculations) is interpreted to pinchout at 6400' based on seismic lap relationships onto the salt.

Buoyancy pressure profiles (Figure 20) are used to perform static trap capacity estimates for buoyant fluids (Bretan and Yielding, 2005). In buoyancy pressure profiles, the fault, separating a charging trap and an uncharged brine (Figure 20A), is progressively filled (A→C) to the limits of the estimated fault gouge capillary entry pressure. Fault rock properties (SGR) vary with depth along a single fault (Figure 20B). These fault derived SGR values, adjacent to the reservoir contact with the fault, are

converted to the appropriate capillary entry pressure (Figure 20C) for the charging fluid (Equations 11 & 16).

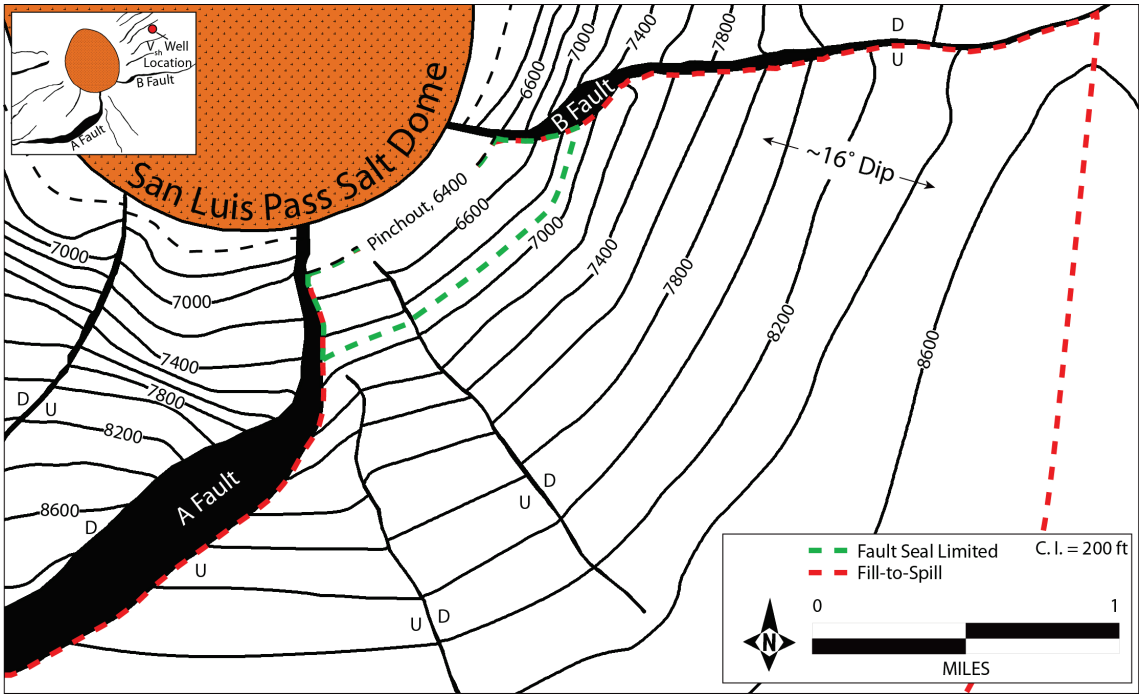

Figure 18. San Luis Pass salt dome, LM2 structure map, SE fault block. Dashed green line represents the limit of membrane fault seal for the LM2 reservoir in the footwall of the B Fault (Area = 175 acres). Dashed red line represents the limits of 'fill-to-spill' for the structure (Area = 2760 acres).

The progressively modeled charges (A→C) create fluid columns with increasing buoyancy pressure (Equation 2) until the buoyancy pressure (column C, Figure 20C) eventually equals the capillary entry pressure of the fault rock, representing the exact weak point on the fault.

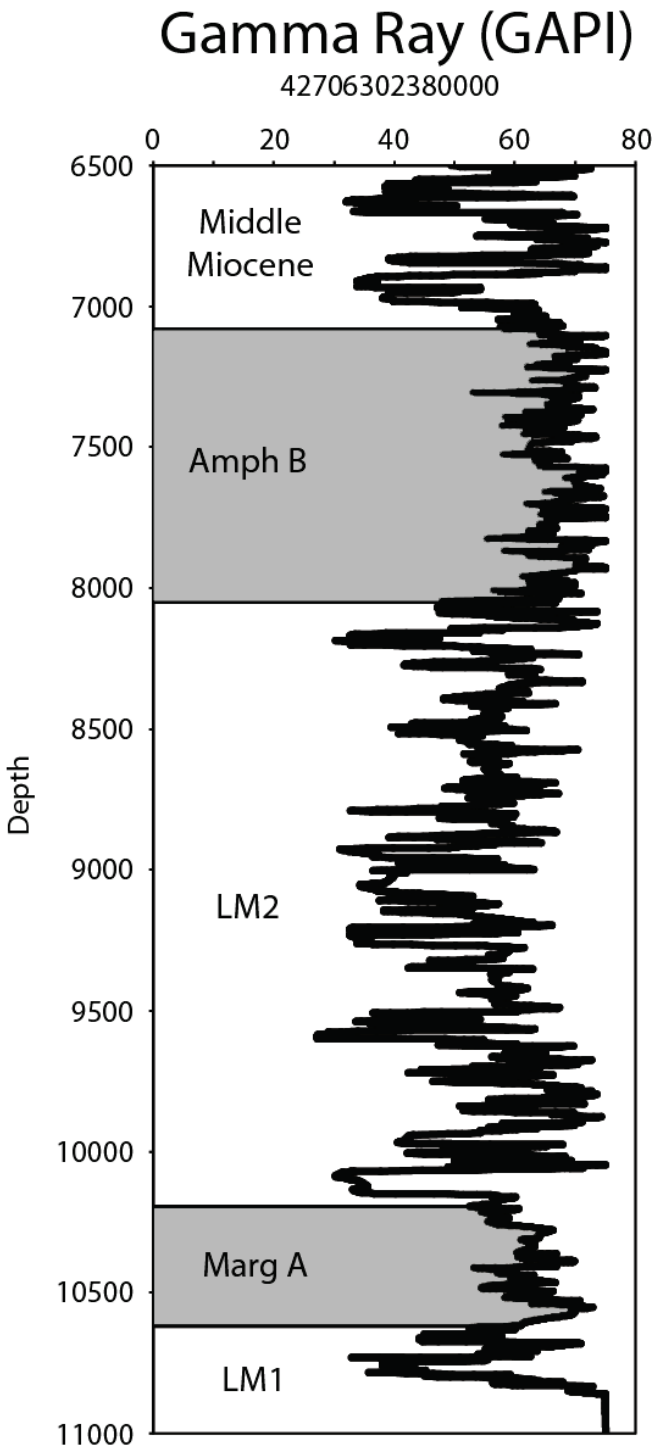

Figure 19. Gamma ray well log type section for the Lower Miocene 1 & 2, San Luis Pass.

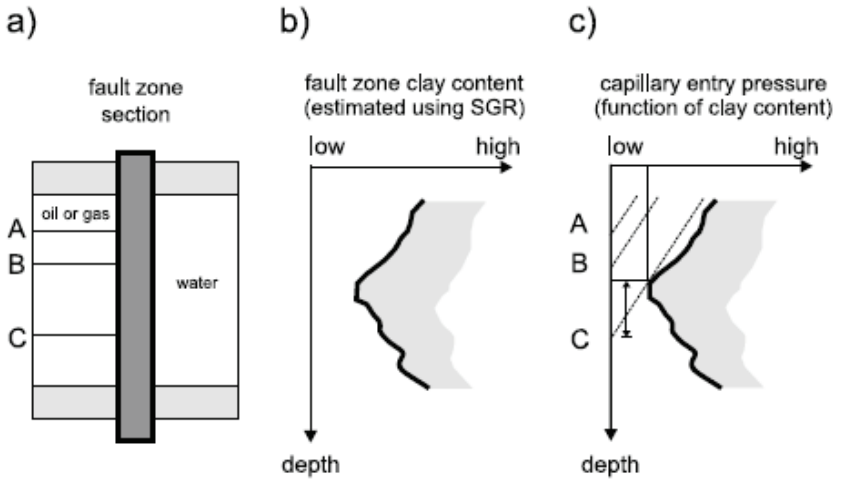

Figure 20. Buoyancy pressure profile schematic. See text for discussion. (a) Fault zone separates a progressively charging trap (A→C) on the left hand side from a water bearing reservoir on the right hand side. (b) The SGR values of the fault zone as they vary with depth. (c) The SGR have been converted to P_{ce} and the pressure exerted by the buoyant columns with depth is represented by A→C, with C representing the maximum column height supported (BP=P_{ce}) by the fault zone properties. Image from Bretan and Yielding (2005).

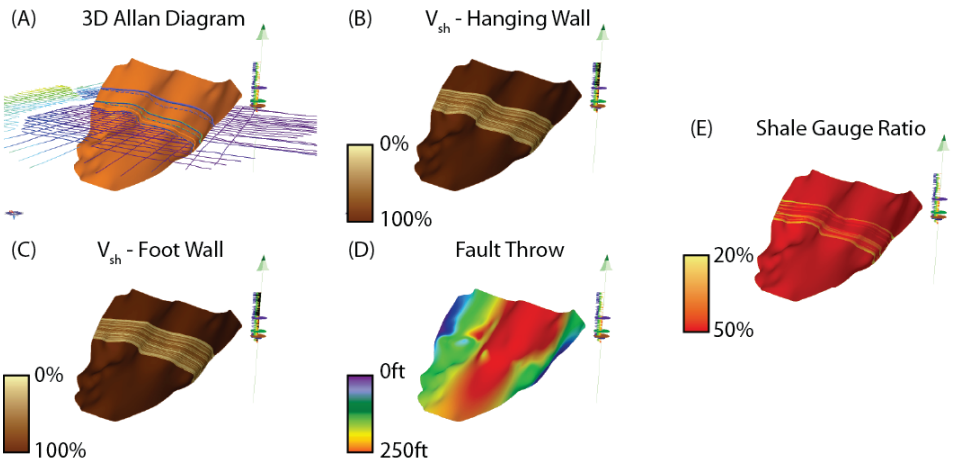

Figure 21. Schematic 3-dimensional fault modeling workflow (A→E). (A) Allan diagrams (Allan, 1989) are constructed from fault and horizon data. (B,C) V_{sh} is calculated for the hanging wall and footwall. (D) Fault throw is modeled from the Allan diagram. (E) Shale gouge ratio is computed from V_{sh} distribution and fault throw.

The workflow applied to the depth-converted 3D seismic volume to map the fault properties required to calculate the SGR requires mapping of the faults and stratigraphic horizons, calculation of Vsh distribution along the fault, and calculating the throw distribution along the fault from the mapped horizons (Figure 21). The SGR values from the LM2 reservoir interval only (adjacent to the footwalls of both the A and B Faults) are calculated and implemented into the following workflow to convert SGR to CO_2-capillary entry pressures.

STATIC CO2-BRINE MEMBRANE FAULT SEAL WORKFLOW SUMMARY

The SGR values must first be converted to mercury-air equivalent capillary entry pressures (Equation 16). Average temperature for the reservoir crest is calculated (Equation 5), reservoir pressure is assumed to be hydrostatic, and the average CO_2 density is calculated using the Peng-Robinson equation of state for the estimated temperature and pressure. CO_2 IFT is then calculated (Equation 9). The mercury-air converted SGR data points are then converted to CO_2 equivalent capillary entry pressures using the calculated CO_2-brine IFT, a contact angle of 0°, and a maximum Miocene salinity value of 1.63m (Equation 11).

Only the SGR values from the footwalls of the A Fault (blue line) and B Fault (red line), LM2 horizon, are considered (Figure 22A). Simulated buoyancy pressures from increasing CO_2 column heights are overlain on the mercury-air equivalent capillary entry pressures to create a buoyancy pressure profile (Figure 22B). Buoyancy pressures

are calculated (Equation 2) using the calculated average CO_2 density of 0.62 g/cm^3 at the reservoir crest depth (6,400') and a brine density of 1.02 g/cm^3. Assumed geologic time scales allow for equilibration (Equation 4) of the injected fluid (i.e. no mechanical leakage).

FAULT SEAL CAPACITY VS FILL-TO-SPILL CAPACITY

The modeled 450 foot CO_2 column height (Figure 22B) reaches the limit of capillary membrane seal of the B Fault. Therefore, the B Fault is the weak-leak point, and the maximum potential CO_2 column height sealed over geologic time is estimated to be 450 ft. The area that this column height would occupy (from top structure at 6,400' to 6,850', green dashed line, Figure 18) is 175 acres. The area associated with a model that fills this trap from fill-to-spill (red dashed line, Figure 18) is 2,760 acres. The fill-to-spill model would overestimate the CO_2 storage capacity by 15.77 times. This is, however, a more extreme example with relatively steep dips where the area increases exponentially down structure. Traps that have shallower dips and become more confined down structure would have less pronounced differences between membrane seal capacity to structural spill capacity and could even yield the same result, or zero difference.

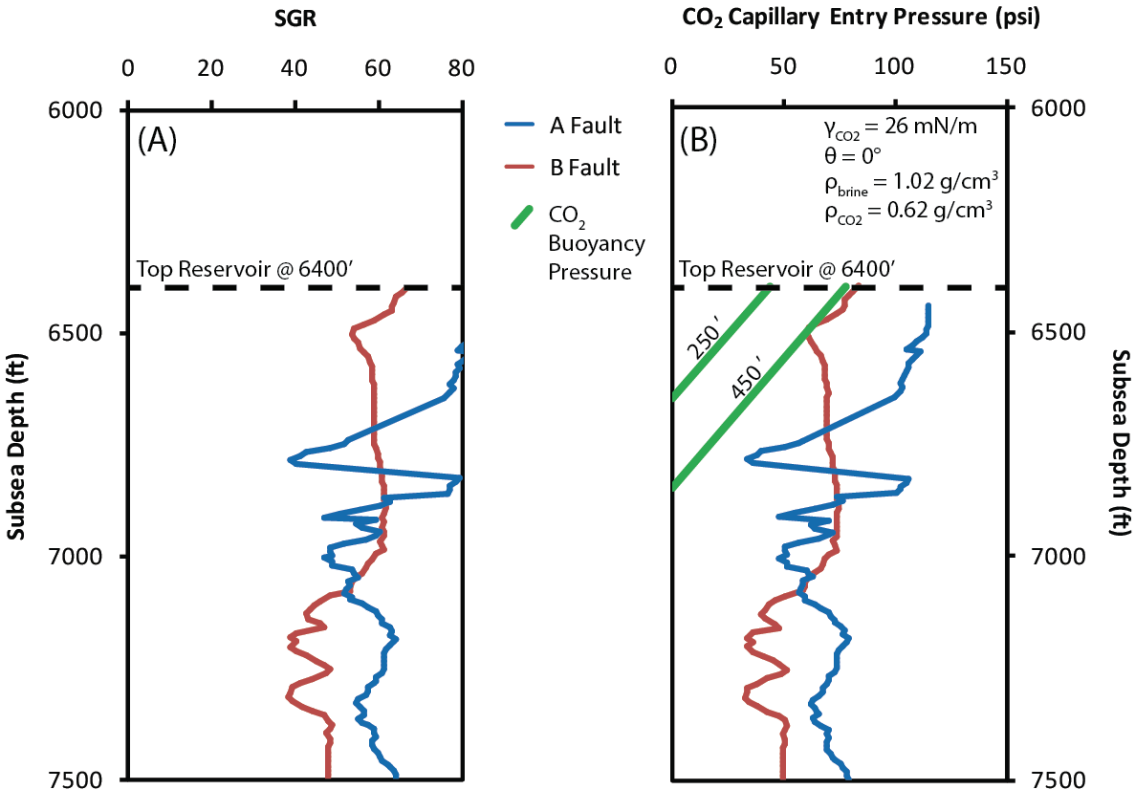

Figure 22. Buoyancy pressure profile LM2, SE fault block, San Luis Pass salt dome. (A) LM2 reservoir interval SGR values from the footwall of both the A Fault and B Fault. (B) Buoyancy pressure profile created from (A) using the workflow: P_{cma} = 25.382 (SGR) - 507.63 and average CO_2 fluid properties from the top-reservoir depth of 6400 ft.

Fault Slip Stability

While membrane fault seal capacity is important for long term containment modeling for CO_2 sequestration, it is also important to model the prospective site for pressure fluctuations to avoid fault reactivation or hydraulic fracturing of the seal. Case studies show that increases in pore pressure from injection of salt water brine adjacent to a fault can reactivate the fault and create small magnitude (M ~2.5 - 3.0) earthquakes (Raleigh et al., 1976; Frohlich et al., 2011). While most faults in the unconsolidated sediments of the Gulf of Mexico have been shown to move by aseismic creep (Frohlich, 1982), regional studies have shown that fault reactivation can lead to hydrocarbon leakage along the fault (Finkbeiner et al., 2001) at potentially high rates (Losh et al., 1999).

The principal stress directions for normal faulting are S_v (σ_1) > S_H (σ_2) > S_h (σ_3), where S_v is the vertical stress, S_H is the maximum principal horizontal stress, and S_h is the minimum principal horizontal stress. These principal stresses create shear stress (τ) parallel to the fault plane and normal stress (σ_n) perpendicular to the fault plane (Figure 23A). The differential stress ($\sigma1$-$\sigma3$) defines the diameter of the Mohr circle and the shear stress and normal stress define the Coulomb failure envelope:

$$\tau = C + \mu(\sigma_n - P_{f)} \ , \qquad (20)$$

where C is cohesion (psi), or the inherent shear strength of the fault gouge, μ is the coefficient of static friction, and P_f is the pore fluid pressure (Jaeger and Cook, 1969; Byerlee, 1978). Cohesion of fault gouge is often considered to be negligible.

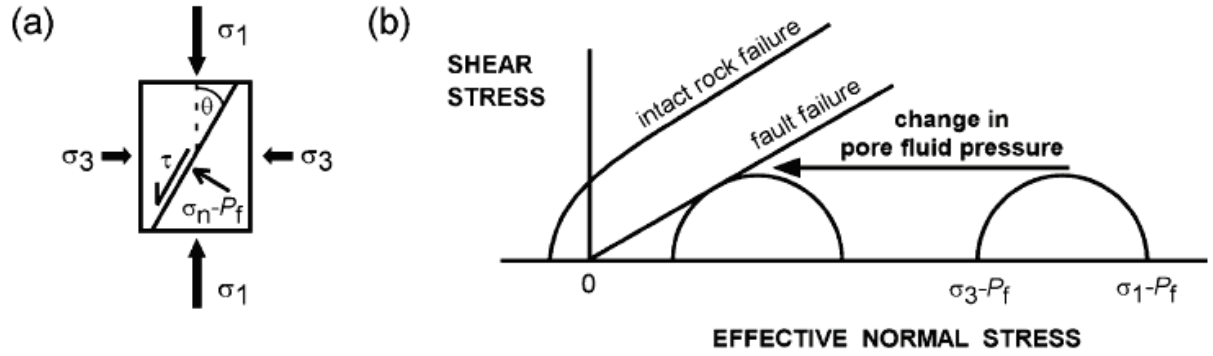

Figure 23. Fault slip stability schematic. (a) Two-dimensional graphic of vertical (σ_1 for normal stress regimes) and horizontal (σ_3) stresses acting on an angled (θ) fault plane to create shear stress (τ) and normal effective stress (σ_n-P_f). (b) Mohr-Coulomb diagram showing the effects of a change in fluid pressure on the effective differential stress. Image from Streit and Hillis (2004).

The coefficient of static friction of fault gouges largely depends on the composite mineralogy of the gouges. Values of 0.6 are reasonable estimates for μ (Shimamoto and Logan, 1981). Increased pore fluid pressure can cause the Mohr circle to move towards, and potentially intersect, the Coulomb failure envelope (Figure 23B). When P_f is increased enough to cause the shear stress on a fault plane to intersect the failure envelope, reactivation of a preexisting fault occurs.

In the absence of 4-arm dipmeter data used for borehole breakout analysis (Moos and Zoback, 1990), regional fault strike statistics (Figure 24) are being substituted to determine the orientation of the principal horizontal stresses. Average fault strike from 297 faults, each broken into 500ft spacing in map view in order to negate bias towards smaller fault traces, yielding 8003 total measurements. These fault strikes have a mean

azimuth of 54.1°. This azimuth roughly parallels the coastline and agrees with onshore determinations of the maximum principal horizontal stress azimuth (Zoback and Zoback, 1980).

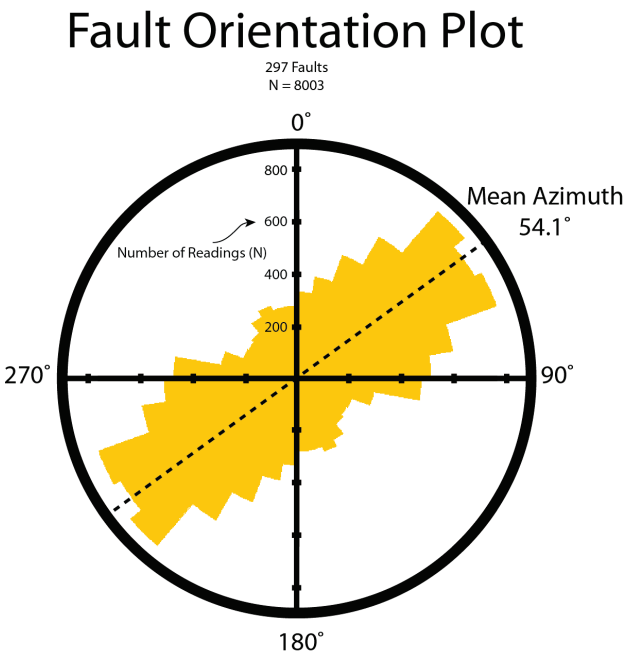

Figure 24. Regional fault strike rose diagram. Fault orientation plot of 297 faults mapped on the LM2 horizon. Each fault is broken into segments at 500' lateral intervals and the average strike is measured to reduce the bias of smaller faults, resulting in 8003 measurements. Mean azimuth of the fault segments is 54.1°.

Using C=0, μ=0.6, σ_1=1.0 psi/ft, σ_3 = 0.85 psi/ft, P_f = 0.445 psi/ft, and an S_H (σ_2) azimuth of 54.1°, the fault slip stability for the A Fault and B Fault have been calculated (Figure 25), respectively, for a depth of -6,600ft (just below the top LM2 reservoir). Since S_H could not be modeled, the two extremes for values of S_H in a normal stress

regime (S_v>S_H>S_h) are modeled: S_H=S_h and S_H=S_v. Regardless of which portion of the fault is most susceptible to slip as a function of increased pore pressures from injection of CO_2, it should be noted that these pore pressure elevations are at minimum ~2500psi, which is two order of magnitude larger than the buoyancy pressure required to overcome the capillary entry pressure of the same faults (Figure 22B). The maximum sustainable pore pressures estimated from fault slip stability analysis should be used as guidelines for best practices in monitoring pressure increases due to CO_2 sequestration.

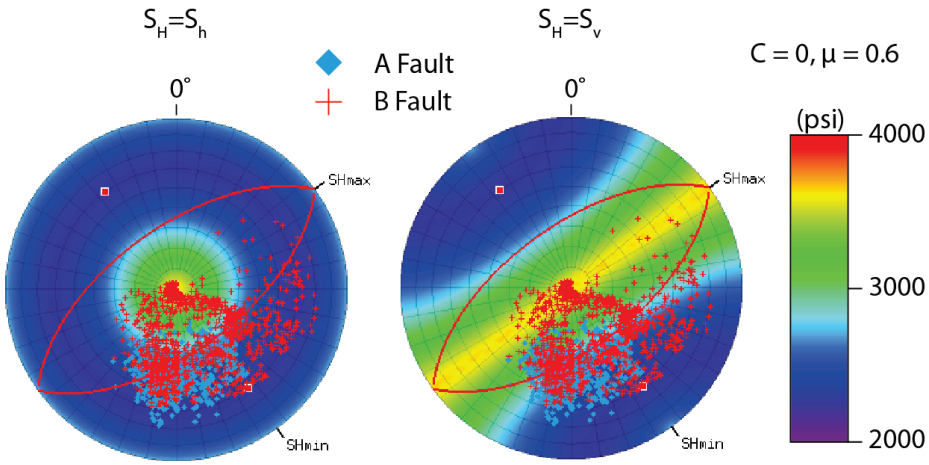

Figure 25. Fault slip stability plots for the A Fault and B Fault. Depth modeled: 6,600ft. Poles to the planes of the A Fault and B Fault are plotted on a lower hemisphere projection. Since there is uncertainty in the value of S_H, the two possible extremes were modeled: (left) S_H=S_h and (right) S_H=S_v.

Modeling of the fault slip stability can have significant error due to unpredictable variations in μ, C, or local stress states (Dewhurst and Jones, 2002). However, even if the critical pore pressure is exceeded, generating aseismic earthquakes in unconsolidated

sediment may not equate to fluid leakage, and if leakage does occur, may only produce flow rates within the upper range of fault zone permeabilities (Wilkins and Naruk, 2007). If uncemented PFFRs or clay smears are the sealing mechanisms, reactivation and displacement may further shear the fault gouge instead of creating a conduit for flow. For example, surface penetrating faults adjacent to an exploration target are often considered to be a detrimental factor that equates to a dry hole. However, fields within the deepwater Gulf of Mexico have surface penetrating faults with active scarps and the same faults trap considerable hydrocarbon columns at depth (Nicholson et al., 2012).

Variability in the SGR Calculation – Sources of Error and Cause for Concern

V_{CL} Calibration

One difficulty with empirical V_{sh} calculations is the consistency of methodology in determining the volume of shale (Bretan et al., 2003). V_{sh} determined from log suites attempt to measure the relative percentages of clay minerals in the rock. However, as can be seen from the effects of cataclasis (in the absence of clay minerals), fault seal is dependent upon maximum interconnected pore throat diameter (Equation 3). In siliciclastics this is primarily dependent on the direct relationship between mineralogy and grain size (pore throat size).

Lateral Stratigraphic Heterogeneity

Lateral stratigraphic heterogeneities can create lateral variability in the SGR calculation for a fault. However, for faults with throws that are orders of magnitude higher than the variable bed thickness in question, small scale stratigraphic heterogeneities become negligible. This effect can be a concern in highly channelized depositional settings, such as in channelized fluvial or turbidite deposits.

Structural Interpretation From Seismic

Faults are often interpreted on seismic data as single continuous planes, when in reality they can exist as complex anastomosing slip surfaces. Fault tip bifurcations can cause splays and multiple closely spaced fault steps (Wehr et al., 2000; Koledoye et al.,

2003). Fault steps can completely alter SGR calculations (Færseth et al., 2007). However, large, seismic scale faults (>100's ft throw) can reduce this uncertainty. Fault steps can also cause blocks of host rock sandstone to be incorporated into the fault core (Loveless et al., 2011). Sandstone boudinaged in the fault gouge cannot be predicted by the SGR algorithm and can provide a potential leakage pathway (Wehr et al., 2000; Færseth et al., 2007).

SEISMIC RESOLUTION AND THE FAULT DAMAGE ZONE

The SGR methodology applies to the fault core itself, or the area between the main slip surfaces. The fault damage zone, or the area flanking the fault core which contains numerous small faults, is often the leakage pathway in carbonate fault rocks, whereas the fault core itself is sealing (Agosta et al., 2007). Siliciclastic faults have been suggested to show similar fault core and fault damage zone geometries, however cataclasites occur in the damage zone instead of fractures (Loveless et al., 2011). Fault statistics can be used to constrain the minimum resolvable fault dimensions and their relationship to other studies of normal faults. Maximum fault trace versus maximum fault displacement data for 297 faults from the LM2 horizon show good agreement with the fault-growth models (F'=3 GPa shear modulus) of Walsh and Watterson (1988) (Figure 26). The important data missing owing to limits in seismic resolution are faults with traces less than 100-200 meters and below (small fault throws). Could these small faults act as the main conduits for leakage? Even if small, seismically irresolvable faults are a potentially dominant leakage mechanism, they are highly unlikely to be both

continuous and surface penetrating. Most likely these small damage zone faults will act as inter-formational leakage mechanisms from the injection reservoir to the next structurally higher reservoir. Acquiring higher resolution seismic surveys for shallower targets can help mitigate this concern.

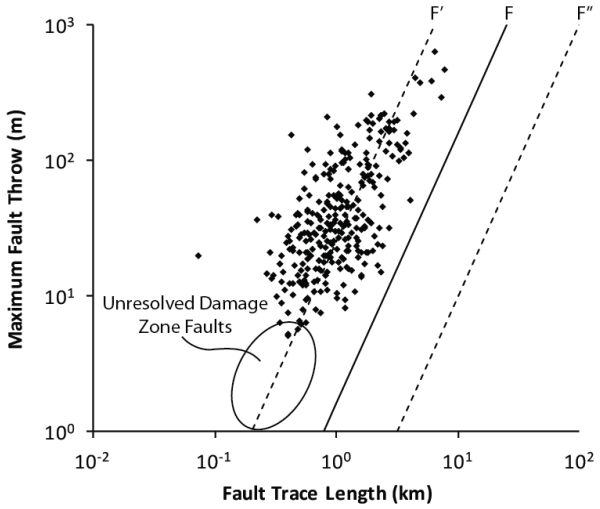

Figure 26. Fault trace length vs maximum fault throw, LM2 horizon. The data are from a regionally depth converted seismic volume and therefore have a minor amount of inherent error from time-to-depth conversion

SMALL THROW ON FAULTS

The SGR has been shown to properly estimate the amount of clay in the fault gouge on large faults (100's m) in the subsurface and even in outcrop (Foxford et al., 1998). Conversely, the SGR for faults with small throw (< 10m), thinly bedded host rock shales (~1-2m), and a high degree of smear have been shown to underestimate the amount of clay in the fault gouge as well as underestimate the sealing potential (Eichhubl

et al., 2005). SGR has also been shown to overestimate the sealing potential of faults with small throw within sandy reservoir intervals thicker than the throw window (Nicholson et al. 2012).

Discussion

While static membrane seal capacity of faulted traps has been shown (e.g. San Luis Pass salt dome) to result in smaller column heights (smaller storage areas) than fill-to-spill modeling of faulted traps on a site specific scale, faulting on a regional scale may actually increase storage potential. For example, if no faults were to exist around the San Luis Pass salt dome, the entire column height required to fill the structure would be limited by the top seal capillary entry (assuming pore pressure is monitored and does not exceed S_h or S_c). However, by introducing faulted compartments the structure of the newly formed traps may have (a) shallower relief, (b) the ability to trap many more, smaller accumulations with a net increase in capacity, and (c) the ability to increase residual trapping by increasing the number of catchments.

Faulted compartments can also increase the capacity volume owing to the rate of charge of the trap. Thus far, time has been referenced only as 'geologic time,' a very ambiguous number, but one that refers to the time scales for which the system can equilibrate to the membrane seal (capillary entry) capacity. This equilibration is the basis for the exploration-style fault seal methodology used for calibration from natural hydrocarbon accumulation. However, if the fault-bound trap is charged with CO_2 to the point where capillary entry pressure is overcome and hydraulic leakage (Watts, 1987) begins to occur, yet reservoir pressure is managed so as not to overcome the fracture or fault-reactivation gradient, time becomes a critical factor in containment. What if the time scale for the equilibration of capillary sealing is 1 million years, but the time interval

of interest for CO_2 containment is only 10,000 years? In this scenario the relative permeability (to CO_2) of the fault and the fault core thickness become the necessary properties to map and simulate. If CO_2 takes 10,000 years to reach the sea floor by upward fault-parallel migration from the injected fault block that has now been slowly filled-to-spill, then the area associated with the fill-to-spill structure is a more accurate assessment of present-day usable capacity. The path forward for modeling fault-bound trap capacity is to use the presented workflow to model fault rock petrophysical properties to be used in a dynamic injection-leak model. Using an SGR fault model converted to CO_2-brine capillary entry pressure, the fault rock mercury-air capillary entry pressure to bulk permeability workflow of Sperrevik et al. (2002), and the relative permeability curves for fault rocks and CO_2 of Tueckmantel et al. (2012), simulations of fault-parallel flow from the injection reservoir to the sea floor can model the time scales for CO_2 leakage from the reservoir to out-of-zone compartments or the sea floor. This will provide a worst-case minimum estimate of storage time.

The static SGR calculated column height workflow is put forth as an empirical methodology to estimate risk in fault bound traps and predict realistic, pre-injection CO_2 capacities. The proposed dynamic fault slip stability and dynamic fault migration workflows are meant to act as guidelines for more detailed CO_2 capacity and containment modeling. However, it should be noted that no field studies or subsurface projects exist on active, purely CO_2-brine injection sites along the Gulf Coast to test the presented fault seal analyses. It is suggested that moving forward, small, field scale tests be conducted in the subsurface on faulted compartments (using both injection and across-fault monitoring

wells) to test the principles of pre-injection fault seal prediction prior to the commencement of commercial scale CO_2 injection into fault bound brine reservoirs.

New Data Contributions

New data contributed to the understanding of membrane fault seal capacity for both methane and CO_2 within the Lower Miocene, Texas State Waters, include:

1. Structural and stratigraphic interpretation of the LM1 and LM2, Matagorda Bay Area.
2. Mapping of the LM2 structure throughout the Texas State Waters and establishment of prospective CO_2 sequestration plays.
3. Evidence of the alignment of the LM2 natural gas fields with faulted structures.
4. Mapping of high risk, near-seafloor penetrating faults.
5. Measurements of fault trace length vs maximum displacement statistics and fault azimuth statistics for the LM2.
6. Compilation of Miocene fluid properties with depth, with the addition of ninety three temperature measurements.
7. Analysis of six Miocene natural gas traps for fault seal calibration. These data are compared with a global fault seal database as well as Miocene top seal capacity from a stratigraphically equivalent section.
8. Development of a comprehensive workflow to analyze static CO_2 membrane fault seal capacity and fault slip stability (reactivation risk) in the Miocene section of the Texas State Waters using the fault seal calibration and fault statistics, respectively.
9. Comparison of static membrane fault seal capacity modeling with fill-to-spill capacity modeling for a potential sequestration site at San Luis Pass salt dome.

Conclusions

Regional play concepts have been established for CO_2 sequestration in the Lower Miocene stratigraphy of the Texas State Waters. All dominant play types involve fault-bounded traps. Regional natural gas trends conform with faulted structures and show that treating faults as no-flow boundaries (fill-to-spill modeling) is not accurate and fault rock properties must be used in modeling long term CO_2 sequestration capacity.

A workflow has been established to calibrate membrane fault seal capacity. Regional temperature, pressure, and salinity data are compiled and used to calculate fluid properties such as fluid density and interfacial tension variability with depth. These fluid properties allow for the calibration of Miocene age fault bound methane columns to calculated fault rock properties (SGR). Fault seal analysis for the Miocene section along the Texas State Waters agrees with published global fault seal databases, but may not be applicable for reservoirs deeper than 3km. Stratigraphically equivalent top seal capacity can be expected to be an order of magnitude higher than fault seal capacity, showing that faults are the limiting factor for capacity estimation for the reservoir studied.

The methane fault seal calibration can be converted to CO_2 equivalent capillary entry pressure for site specific capacity modeling. Modeled results for membrane fault seal capacity at the SE block of the San Luis Pass salt dome, LM2 reservoir, show a large decrease in long term capacity compared with fill-to-spill (structural closure) modeling.

Regional fault mapping and pressure data provide context for the regional state of stress orientation and magnitude, respectively. Fault slip stability modeling shows that

pressure increases two orders of magnitude greater than the buoyancy pressure retained over geologic time scales are required to potentially cause fault reactivation and leakage. There is no certainty that fault reactivation will cause leakage, but these pressure increases provide a good estimate for the maximum allowable increase in reservoir pressure during short-term injection time scales.

Membrane fault seal and fault slip stability workflows established for the Lower Miocene in the Texas State Waters can be used to quantify column heights and storage capacities for both site specific and regional capacity estimations.

Appendix A

Checkshot and synthetic seismogram data for seismic depth conversion.

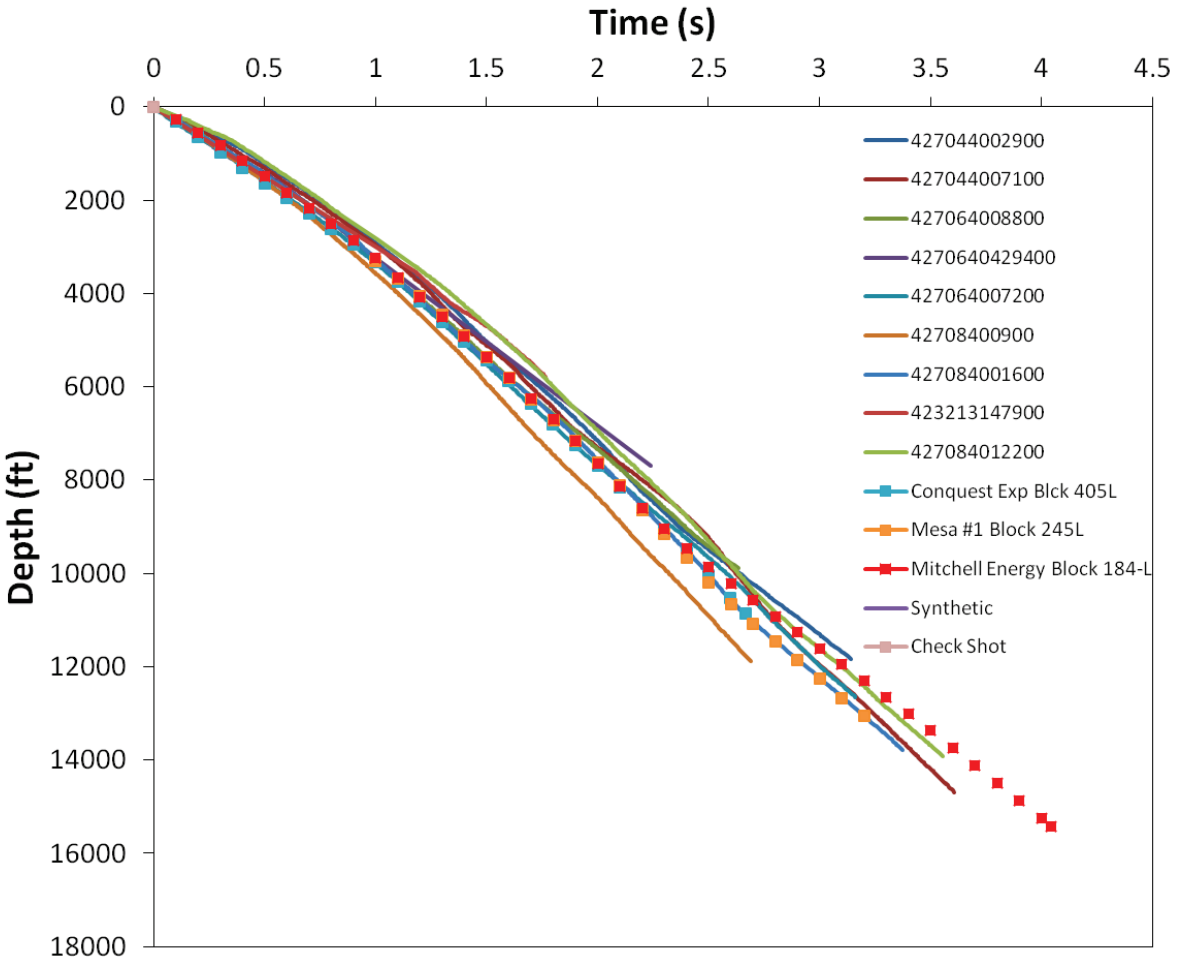

Appendix B

Texas Gulf Coast (onshore and offshore) Miocene brine salinity values (mg/L) from Breit (2006)

UNIQID	LAT	LONG	API	WELLNAME	MAX DEPTH	CHLORIDE	SODIUM
42019021	27.38	-98.52		WELDER HEIRS GAS UNIT 1 #1T	8160	19500	12362
42004178	27.47	-98.00	4227301175	K. R. BORREGOS 311		6496	5610
42017995	27.47	-97.04		COPANO STATE 74-6	7190	9289	6508
42018009	27.47	-97.08		COPANO STATE 104-7	6930	30622	18263
42017985	27.47	-97.04		COPANO STATE 68-7	7212	12736	8732
42017994	27.47	-97.04		COPANO STATE 74-7	7110	16317	10379
42018038	27.47	-97.08		COPANO STATE 76-4	6642	33145	19680
42018039	27.47	-97.08		COPANO STATE 76-4	6717	30690	18318
42017565	26.35	-98.59		RINCON GASOLINE PLANT NO. 38	900	468	459
42253856	26.71	-98.47	4242731328	I V MONTALVO C-#39	6550	40410	23225
42253917	26.39	-98.56		CHAPOTAL LACT UNIT		15871	10021
42008853	26.41	-98.54		M. SAENZ ST. NO. 17	6123	7839	4294
42008880	26.41	-98.54		M. SAENZ STATE #14	6146	7460	4462
42009585	28.61	-94.32		SUN FEE UNIT #1-C		77415	42179
42009685				H. R. HOUCK #1	2593	5452	3408
42009798				I. D. ISENSEE # 2		52750	30723
42010465	26.31	-97.57		#78 SAUZ RANCH MULATOS PASTURE	4360	85500	46849
42010596	28.80	-94.18		#13 TREADAWAY LAND COMPANY	5310	62500	39000
42010597	28.75	-94.07		#202 W. P. H. MCFADDIN	3238	72500	40000
42010826	28.54	-94.11		MCFADDIN STATE NO. 14-VT	5882	71536	42516
42014729	26.18	-98.57		PHILLIPS - T. F. VILLARAL #2	4134	8076	NA
42014731	26.18	-98.57		PHILLIPS - TOWN #1	3901	18224	NA

42015311	28.75	-94.40		A. M. CARPENTER #10	4426	67732	36890
42015315	28.54	-94.11		MCFADDIN TRUST #15	3927	69647	40338
42015340	28.54	-94.11		MCFADDIN TRUST #30	4743	23328	NA
42015352	28.71	-94.12		E. PLEASANT ET AL #1	7807	19558	NA
42015654	28.51	-95.25		A. P. HOWARD #2		57188	26921
42015949	28.33	-94.95		SOUTH GILLOCK WATER FLOODING SYSTEM #1		79925	45441
42018976	30.23	-94.23		ARRIOLA FEE #28	2697	10820	6400
42018978	30.23	-94.23		ARRIOLA X LEE - WELL #5	3232	45600	25100
42250080	29.44	-96.48	4208900953	W N LEHNER #1	1986	1190	838
42250140	29.56	-94.40	4216700523	CADE A/A #171	5218	89300	51122
42250149	29.66	-95.24	4220106165	DRILLING DIST 24 #2	4047	45400	21790
42250155	29.74	-94.24	4224530031	TEXAS EXPLORATION CO #20	4442	72300	42431
42250156	30.02	-94.08	4224500833	GLADYS CITY #137	4898	68100	40554
42250157	30.02	-94.06	4224503058	MCFADDIN #226	3888	72000	43459
42250158	30.02	-94.08	4224500838	GLADYS CITY #142	4938	66000	39003
42250159	29.74	-94.25	4224503130	TEXAS EXPLORATION CO #1	4307	78000	46783
42250160	30.01	-94.08	4224503135	GLADYS CITY #154	1917	56000	30695
42250161	30.01	-94.06	4224530203	MCFADDIN #237	3750	62400	36310
42250165	29.74	-94.26	4224502819	HENRY SCHMIDT #7	6794	79100	45429
42250166	30.01	-94.07	4224503109	NEAREN #1	3524	63500	40480
42250167	30.01	-94.07	4224503150	FEE GUILMARTIN #32	3836	121000	76350
42250550				CADE A/A #254	6626	106000	57844
42250552	29.38	-94.95		SOUTH GILLOCK UNIT #502	4498	72000	39451
42250553				CADE A/A #252	5315	104000	59070
42250574				E K CADE B R/A A #43	4684	90800	49431
42250579	29.83	-94.91		CHAMBERS CO AGRIC CO #34	4782	78000	41217

42250596	29.49	-95.23	4203930166	GHOTE #16	4310	2080	1327
42250636	29.65	-95.25		SCHWARZ #5	3865	52500	24397
42250638	29.65	-95.25		DRILLING DISTRICT 4 #1	3750	40400	18761
42250708				WILLAMAR EAST UNIT #20		82600	44453
42250727				WILLAMAR EAST UNIT #21		82300	44178
42250734				WILLAMAR EAST UNIT #20		82600	44502
42250738				WILLAMAR EAST UNIT #21		82300	44227
42250741				WILLAMAR EAST UNIT #20		82600	44463
42250742				WILLAMAR EAST UNIT #20		82600	44511
42250745	26.43	-97.57		WILLAMAR EAST UNIT #20		83700	45666
42250746				WILLAMAR WEST UNIT #2	2800	69500	38180
42250748				WILLAMAR EAST UNIT #20		82600	44472
42250750	26.39	-97.58		WILLAMAR WEST UNIT #1	2800	73400	40329
42251194	29.15	-95.79	4203930823	WISCH SAINT UNIT #6L	7996	47897	28802
42251195	29.15	-95.79	4203930823	WISCH SAINT UNIT #6L	7996	48314	29052
42251196	29.15	-95.79	4203930823	WISCH-SAINT UNIT #6L	7996	59802	35775
42251352	29.48	-94.55	4216700920	ZINN AND FORMAN NO 9		66014	33061
42251444	29.80	-94.15	4224530300	BROWSSARD AND HEBERT NO 35		81585	47089
42251445	29.80	-94.15	4224530441	BROUSSARD & HEBERT #36		80758	45570
42251448	29.80	-94.15	4224502077	BROUSSARD AND HEBERT NO 10		73055	41931
42251971	29.16	-96.81	4228530489	O R BORCHER A #5	2522	663	497
42252371	29.79	-94.14		SPALDING OAKLEY C NO 4		66873	37676
42252372	29.79	-94.14		BROUSSARD AND HEBERT NO 4		70406	40217
42253549	29.80	-94.15	4224502080	BROUSSARD & HEBERT #13	6803	81726	46545
42253939	26.39	-98.56		GARCIA L & L B #7		9711	6729
42254055	26.69	-98.48	4242700592	I V MONTALVO C 24 UT	4305	24157	13851
42254572	27.51	-97.88		E A WERNECKE NO 3	7468	13096	7908

42255777	26.38	-98.57	4242704629	CHAPOTOL LAND CO A #16	4915	8863	5738
42256950	29.31	-95.56	4203901890	RAMSEY B NO 6C		71400	40900
42256953	29.31	-95.56		KEMPNER-REISS NO 1	4690	62916	34684
42256955				RAMSEY B NO 110		150400	95270
42257356	29.70	-94.10	4224502939	MCFADDINS TRUST NO 19	5920	71936	42999
42257357	29.69	-94.10	4224502940	MCFADDIN TRUST NO 21	6130	71936	42566
42257358	29.70	-94.11	4224502943	MCFADDIN TRUST NO 24	4760	78336	46915
42257360	29.69	-94.10	4224502940	MCFADDIN TRUST NO 21		75620	45140
42257362	29.70	-94.10	4224502945	MCFADDIN TRUST NO 26		77842	46494
42257363	29.69	-94.10	4224502953	MCFADDIN TRUST NO 34		73186	42598
42257364	29.70	-94.10	4224502942	TRUST NO 23		71100	42180
42257365	29.70	-94.10	4224502948	MCFADDIN TRUST NO 29	5920	68200	40900
42257366	29.69	-94.10	4224502944	MCFADDIN TRUST NO 25		63900	39000
42257367	29.70	-94.10	4224502929	MCFADDIN TRUST NO 8	5949	72192	42994
42257372	29.76	-93.98	4224503122	MCFADDIN RANCH NO 1		22200	13770
42257374	29.69	-94.11	4224530269	MCFADDIN TRUST STATE NO 30	4743	78861	47095
42257376	29.88	-94.06	4224501622	MCFADDIN STATE NO 1		60091	33831
42257385	29.99	-94.41		A M CARPENTER NO 10	4426	67962	37010
42257390	29.69	-94.10	4224502940	MCFADDIN TRUST NO 21		70518	42083
42257391	29.70	-94.10	4224502955	MCFADDIN TRUST NO 36		74205	44569
42257394	29.69	-94.11	4224502985	MCFADDIN STATE NO 1	2397	61952	35324
42257396	29.71	-94.10	4224502992	MCFADDIN STATE NO 2	3800	72390	40000
42257402	29.70	-94.10	4224502948	MCFADDIN TRUST NO 29	5920	66500	39800
42257403	29.70	-94.11		MCFADDIN TRUST & STATE NO 13		58545	32992
42257410	29.70	-94.11		MCFADDIN TRUST NO 5	3838	73984	44316
42257412	29.70	-94.11		MCFADDIN STATE NO 5		74205	44374
42257414	29.70	-94.11		MCFADDIN TRUST	5914	73186	43445

42257428	29.70	-94.11		MCFADDIN TRUST NO 15	5592	71628	42442
42257429	29.70	-94.11		MCFADDIN STATE NO 4	5948	81026	47552
42257430	29.70	-94.11		MCFADDIN TRUST NO 1T	6464	38400	21288
42257431	29.70	-94.11		MCFADDIN TRUST NO 3	3812	73216	42585
42257434	29.70	-94.11		MCFADDIN STATE NO 4-T	5948	72771	43440
42257436	29.70	-94.11		MCFADDIN TRUST NO 30	2394	61557	34751
42257926	28.03	-97.38		G W PULLIN NO 7	4365	47286	27198
42258401	30.02	-94.06	4224503047	MCFADDIN #215	3675	67000	38933

Appendix C

Reservoir properties and structure maps (with fluid contacts) were obtained from Seni et al. (1997).

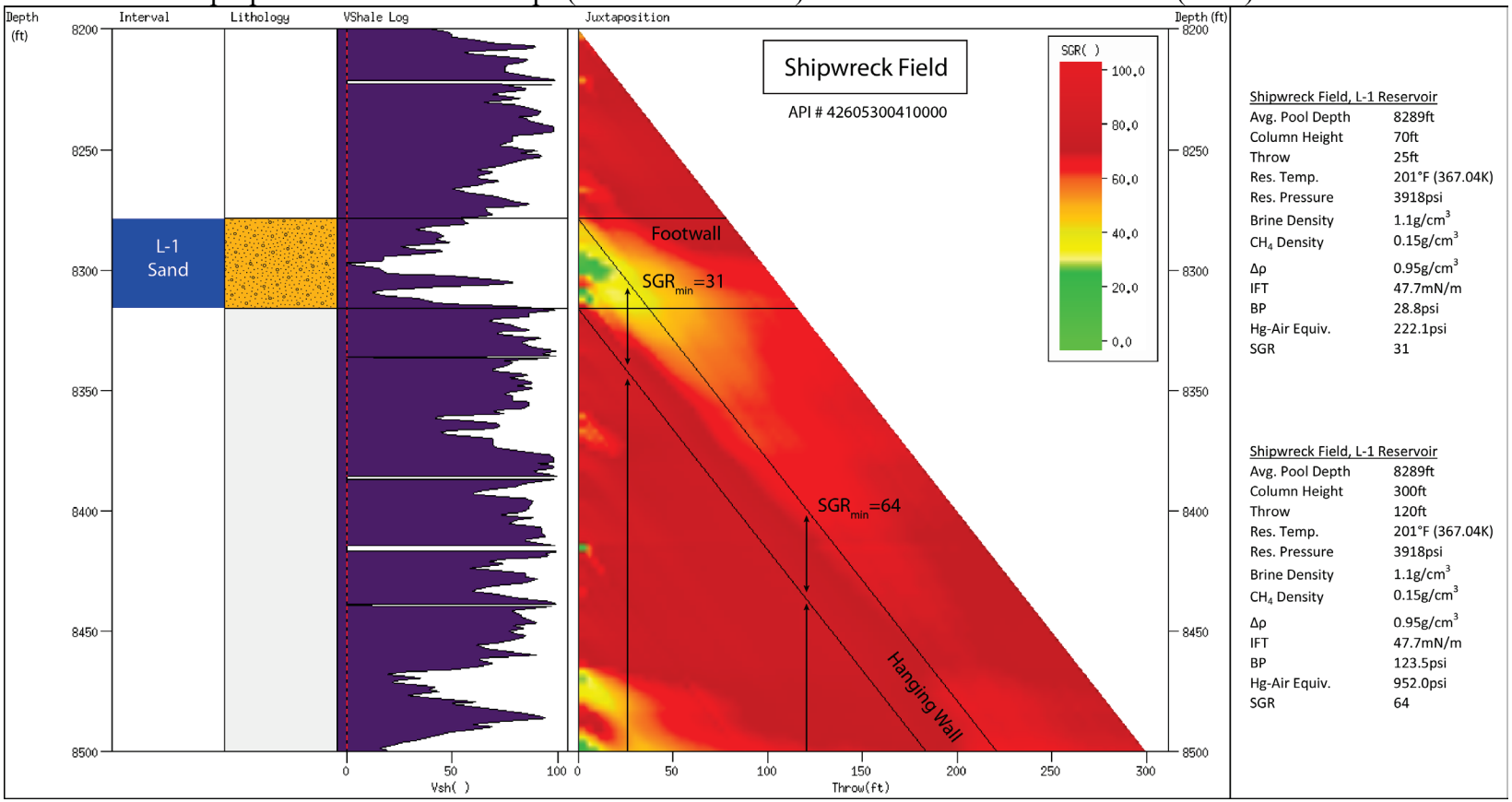

Shipwreck Field, L-1 Reservoir

Avg. Pool Depth	8289ft
Column Height	70ft
Throw	25ft
Res. Temp.	201°F (367.04K)
Res. Pressure	3918psi
Brine Density	1.1g/cm^3
CH_4 Density	0.15g/cm^3
Δρ	0.95g/cm^3
IFT	47.7mN/m
BP	28.8psi
Hg-Air Equiv.	222.1psi
SGR	31

Shipwreck Field, L-1 Reservoir

Avg. Pool Depth	8289ft
Column Height	300ft
Throw	120ft
Res. Temp.	201°F (367.04K)
Res. Pressure	3918psi
Brine Density	1.1g/cm^3
CH_4 Density	0.15g/cm^3
Δρ	0.95g/cm^3
IFT	47.7mN/m
BP	123.5psi
Hg-Air Equiv.	952.0psi
SGR	64

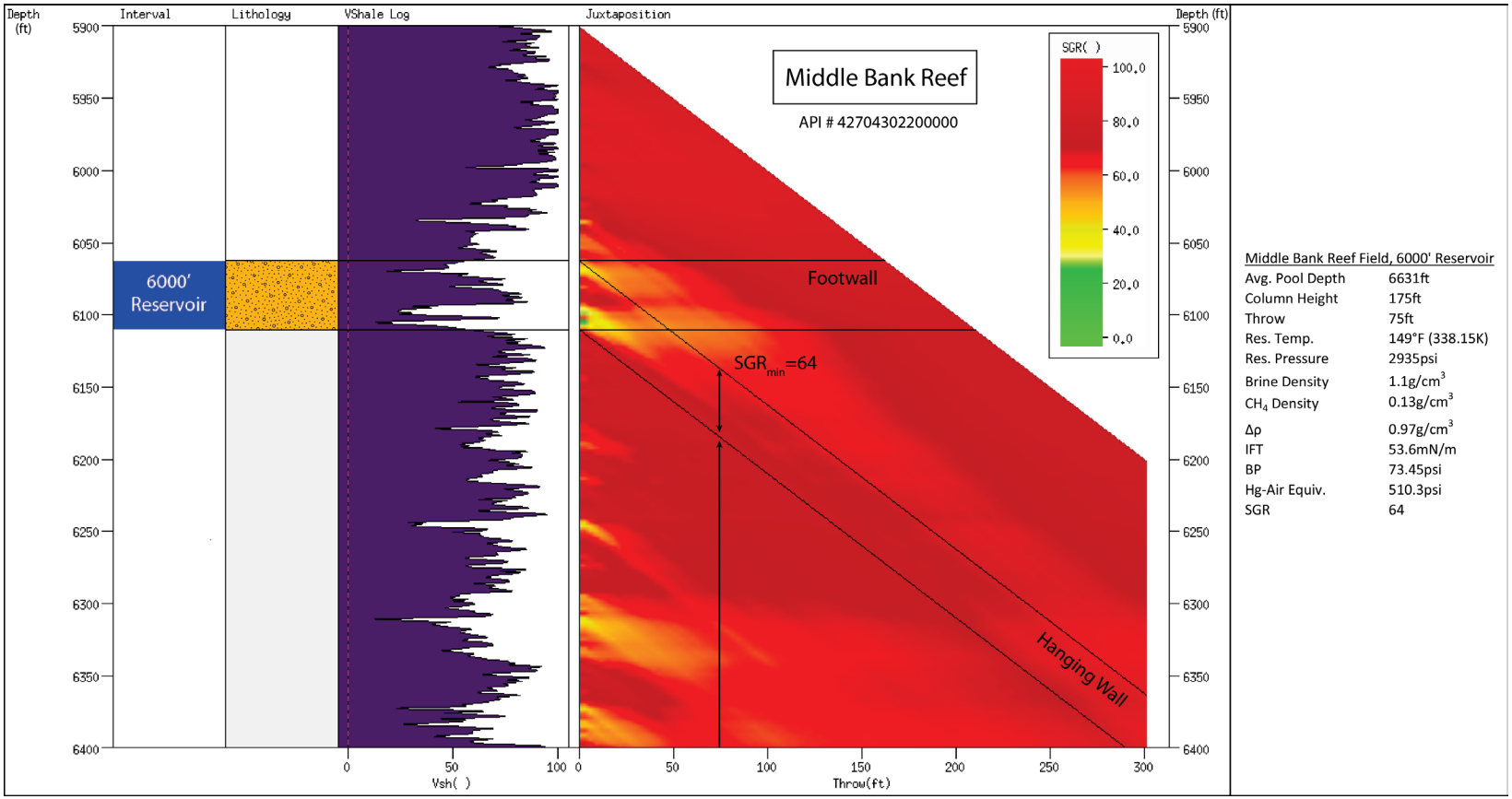

Middle Bank Reef Field, 6000' Reservoir	
Avg. Pool Depth	6631ft
Column Height	175ft
Throw	75ft
Res. Temp.	149°F (338.15K)
Res. Pressure	2935psi
Brine Density	1.1g/cm^3
CH_4 Density	0.13g/cm^3
Δρ	0.97g/cm^3
IFT	53.6mN/m
BP	73.45psi
Hg-Air Equiv.	510.3psi
SGR	64

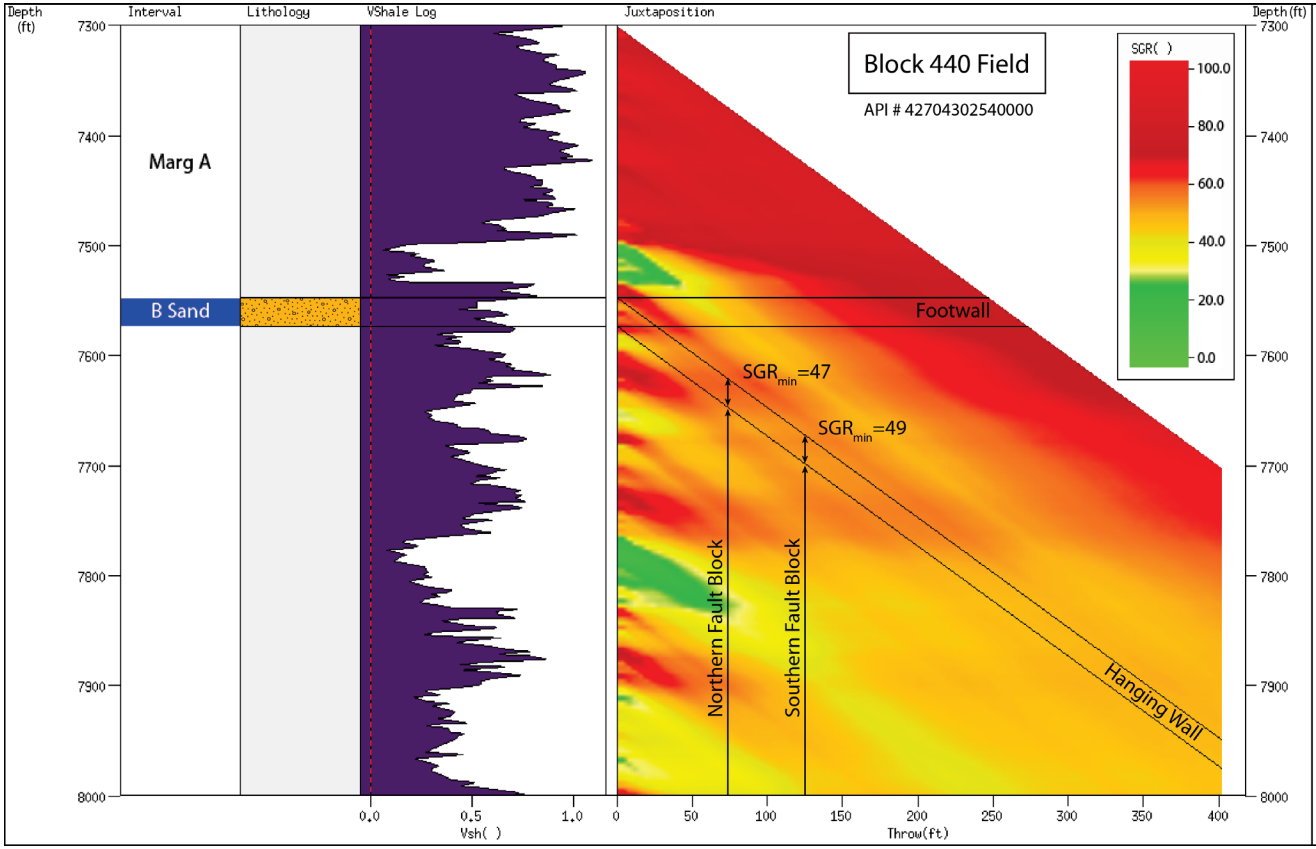

Block 440 Field, B Sand, Southern Fault Block

Avg. Pool Depth	8125ft
Column Height	200ft
Throw	125ft
Res. Temp.	167°F (348.15K)
Res. Pressure	3642psi
Brine Density	1.1g/cm^3
CH_4 Density	0.15g/cm^3
Δρ	0.95g/cm^3
IFT	50.89mN/m
BP	82.13psi
Hg-Air Equiv.	593.6psi
SGR	49

Block 440 Field, B Sand, Northern Fault Block

Avg. Pool Depth	8125ft
Column Height	360ft
Throw	75ft
Res. Temp.	167°F (348.15K)
Res. Pressure	3642psi
Brine Density	1.1g/cm^3
CH_4 Density	0.15g/cm^3
Δρ	0.95g/cm^3
IFT	50.89mN/m
BP	147.86psi
Hg-Air Equiv.	1068.49
SGR	47

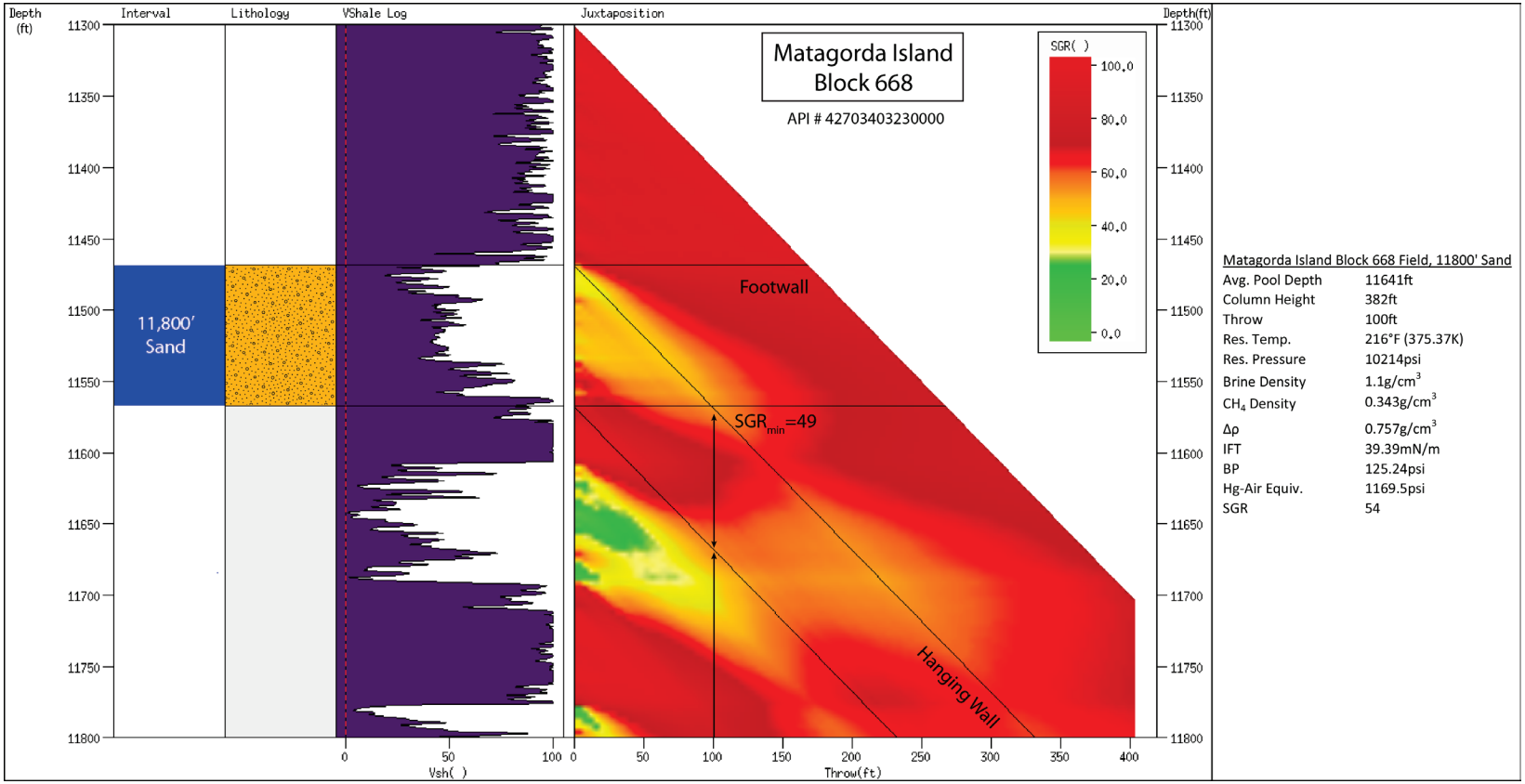
Depth (ft)
Interval
Lithology
VShale Log
Juxtaposition
Depth(ft)
Matagorda Island Block 668
API # 42703403230000
SGR( )
100.0
80.0
60.0
40.0
20.0
0.0
11,800' Sand
Footwall
SGR$_{min}$=49
Hanging Wall
11300
11350
11400
11450
11500
11550
11600
11650
11700
11750
11800
0
50
100
Vsh( )
0
50
100
150
200
250
300
350
400
Throw(ft)
Matagorda Island Block 668 Field, 11800' Sand
Avg. Pool Depth 11641ft
Column Height 382ft
Throw 100ft
Res. Temp. 216°F (375.37K)
Res. Pressure 10214psi
Brine Density 1.1g/cm^3
CH_4 Density 0.343g/cm^3
Δρ 0.757g/cm^3
IFT 39.39mN/m
BP 125.24psi
Hg-Air Equiv. 1169.5psi
SGR 54

Appendix D

Reservoir properties and structure maps (with fluid contacts) used to calculate column height were obtained from Seni et al. (1997).

Reservoir	Pool Depth	Temp (°F)	Temp (°K)	Pressure (psi)	Hydro Equiv (psi)	Sv Equiv (psi)	% Overpressure	Col. Ht.	CH4 ρ	Δρ	BP (psi)	CH4 IFT	Hg/Air
High Island Block 24L GP	7962	154	340.93	3428	3543	7962	0	100	0.15	0.90	39.03	50.37	285.03
West Cameron 66 HG	6505	167	348.15	2822	2895	6505	0	30	0.12	0.93	12.08	50.17	88.54
Brazos Area 446-L SE-4 4200 SD	4134	125	324.82	1459	1840	4134	0	75	0.07	0.98	31.89	56.91	206.10
Middle Bank Reef 6000 Reservoir	6631	149	338.15	2935	2951	6631	0	175	0.13	0.92	69.66	51.61	496.46
Block 440 B Sand FBB	8125	167	348.15	3642	3616	8125	1	360	0.15	0.90	140.03	48.94	1052.34
Block 440 B Sand FBD	8125	167	348.15	3642	3616	8125	1	200	0.15	0.90	77.80	48.94	584.63
Eugene Island 24 1500	14928	281	411.48	6897	6643	14928	3	275	0.20	0.85	101.15	38.15	975.25
Vermilion Block 14 Cib Op	10268	219	377.04	4790	4569	10268	4	75	0.17	0.88	28.58	43.65	240.81
Matagorda Island 703 FT	8947	195	363.71	4175	3981	8947	4	200	0.16	0.89	77.09	46.04	615.90
South Marsh Island 241 B2	7011	151	339.26	3275	3120	7011	4	60	0.14	0.91	23.54	50.87	170.23
Matagorda Island 604 6550	6697	150	338.71	3129	2980	6697	4	160	0.14	0.91	63.16	51.20	453.78
Mustang Island 805 LMA1	9388	194	363.15	4390	4178	9388	4	415	0.17	0.88	158.70	45.86	1272.71
Matagorda Island 527 E	9103	205	369.26	4280	4051	9103	5	350	0.16	0.89	134.93	45.18	1098.48
Shipwreck L-1 Reservoir	8289	201	367.04	3918	3689	8289	5	300	0.15	0.90	116.97	45.89	937.45
Shipwreck L-1 Reservoir	8289	201	367.04	3918	3689	8289	5	70	0.15	0.90	27.29	45.89	218.74
Main Pass 73	13375	247	392.59	6337	5952	13375	5	160	0.20	0.85	58.93	40.50	535.25
Galveston 393 BH-15	6125	162	345.37	2967	2726	6125	7	40	0.13	0.92	15.98	50.38	116.62
Matagorda Island 4A 5050	4999	129	327.04	2446	2225	4999	8	60	0.12	0.93	24.27	54.44	163.99
Brazos 70A TW1	6785	162	345.37	3429	3019	6785	11	300	0.15	0.90	117.48	49.67	869.84

Sabine Pass 10 MP3	11832	221	378.15	6389	5265	11832	17	375	0.21	0.84	136.47	42.07	1193.06
Mustang Island 31A 9700	9114	210	372.04	5274	4056	9114	24	433	0.19	0.86	161.93	43.79	1360.14
West Cameron 68D	16350	283	412.59	12710	7276	16350	60	260	0.29	0.76	85.78	35.16	897.44
South Marsh Island 9	15664	276	408.71	12234	6970	15664	61	810	0.28	0.77	268.41	35.69	2766.33
Mustang Island 31A MP4	11930	253	395.93	9446	5309	11930	62	500	0.25	0.80	172.15	38.17	1658.83
OCS Matagorda Island 668 KQ	11056	202	367.59	8961	4920	11056	66	300	0.27	0.78	101.88	41.47	903.60
East Cameron 60 PQ	14100	273	407.04	11859	6275	14100	71	624	0.28	0.77	207.73	35.99	2122.97
Vermilion Block 14 Rob Sands	13224	261	400.37	11200	5885	13224	72	125	0.28	0.77	41.85	36.89	417.25
Eugene Island 136 PP	18800	310	427.59	15980	8366	18800	73	470	0.31	0.74	150.06	32.84	1680.82
Matagorda Island Block 668 11800 Sand	11641	216	375.37	10214	5180	11641	78	382	0.34	0.71	116.97	37.50	1147.34

References

Agosta, F., M. Prasad, and A. Aydin, 2007, Physical properties of carbonate fault rocks, fucino basin (Central Italy): implications for fault seal in platform carbonates: Geofluids, v. 7, p. 19-32.

Alexander, L. L., and J. W. Handschy, 1998, Fluid flow in a faulted reservoir system: Fault trap analysis for the Block 330 field in Eugene Island, South Addition, offshore Louisiana: Aapg Bulletin-American Association of Petroleum Geologists, v. 82, p. 387-411.

Allan, U. S., 1989, Model for hydrocarbon migration and entrapment within faulted structures: AAPG Bulletin, v. 73, p. 803-811.

Ambrose, W. A., C. Breton, M. H. Holtz, V. Nunez-Lopez, S. D. Hovorka, and I. J. Duncan, 2009, CO2 source-sink matching in the lower 48 United States, with examples from the Texas Gulf Coast and Permian Basin: Environmental Geology, v. 57, p. 1537-1551.

Antonellini, M., and A. Aydin, 1994, Effect of faulting on fluid-flow in porous sandstones - petrophysical properties: AAPG Bulletin, v. 78, p. 355-377.

Argaud, M. J., 1993, Predicting the interfacial-tension of brine/gas (or condensates) systems: Advances in Core Evaluation Iii - Reservoir Management: Reviewed Proceedings of the Society of Core Analysts Third European Core Analysis Symposium, v. 3, 147-174 p.

Atkins, P. W., and L. L. Jones, 2005, Chemical Principles, The Quest for Insight: New York, W.H. Freeman and Company.

Barnes, C., and M. Koretsky, 2003, ThermoSolver (Version 1.0), http://cbee.oregonstate.edu/education/Thermosolver/, John Wiley & Sons, Inc.

Berg, R. R., and A. H. Avery, 1995, Sealing properties of tertiary growth faults, Texas Gulf-Coast: AAPG Bulletin, v. 79, p. 375-393.

Bhuyan, K., and Q. R. Passey, 1994, Clay estimation from GR and neutron-density porosity logs: SPWLA 35th Annual Logging Symposium.

Bouvier, J. D., C. H. Kaarssijpesteijn, D. F. Kluesner, C. C. Onyejekwe, and R. C. Vanderpal, 1989, 3-Dimensional seismic interpration and fault sealing investigations, Nun River Field, Nigeria: AAPG Bulletin, v. 73, p. 1397-1414.

Bradshaw, B. E., and J. S. Watkins, 1994, Growth-fault evolution in offshore Texas: Gulf Coast Association of Geological Societies Transactions, v. 44, p. 103-110.

Bradshaw, J., S. Bachu, D. Bonijoly, R. Burruss, S. Holloway, N. P. Christensen, and O. M. Mathiassen, 2007, CO2 storage capacity estimation: Issues and development of standards: International Journal of Greenhouse Gas Control, v. 1, p. 62-68.

Breit, G., 2006, Produced Waters Database, USGS.

Bretan, P., and G. Yielding, 2005, Using buoyancy pressure profiles to assess uncertainy in fault seal calibration: AAPG Hedberg Series, v. 2, p. 151-162.

Bretan, P., G. Yielding, and H. Jones, 2003, Using calibrated shale gouge ratio to estimate hydrocarbon column heights: AAPG Bulletin, v. 87, p. 397-413.

Bretan, P., G. Yielding, O. M. Mathiassen, and T. Thorsnes, 2011, Fault-seal analysis for CO2 storage: an example from the Troll area, Norwegian Continental Shelf: Petroleum Geoscience, v. 17, p. 181-192.

Brown, A., 2003, Capillary effects on fault-fill sealing: AAPG Bulletin, v. 87, p. 381-395.

Byerlee, J., 1978, Friction of rocks: Pure and Applied Geophysics, v. 116, p. 615-626.

Chalbaud, C., M. Robin, and P. Egermann, 2006, Interfacial tension data and correlations of brine-CO2 systems under reservoir conditions: SPE Annual Technical Conference and Exhibition.

Childs, C., Ø. Sylta, S. Moriya, J. J. Walsh, and T. Manzocchi, 2002, A method for including the capillary properties of faults in hydrocarbon migration models: Norwegian Petroleum Society Special Publications, v. 11, p. 127-139.

Chiquet, P., D. Broseta, and S. Thibeau, 2007a, Wettability alteration of caprock minerals by carbon dioxide: Geofluids, v. 7, p. 112-122.

Chiquet, P., J.-L. Daridon, D. Broseta, and S. Thibeau, 2007b, CO2/water interfacial tensions under pressure and temperature conditions of CO2 geological storage: Energy Conversion and Management, v. 48, p. 736-744.

Davies, R. K., L. J. An, P. Jones, A. Mathis, and C. Cornette, 2003, Fault-seal analysis South Marsh Island 36 field, Gulf of Mexico: AAPG Bulletin, v. 87, p. 479-491.

Dewhurst, D. N., and R. M. Jones, 2002, Geomechanical, microstructural, and petrophysical evolution in experimentally reactivated cataclasites: Applications to fault seal prediction: AAPG Bulletin, v. 86, p. 1383-1405.

Divko, L. M. G., J. Hamilton, and G. W. O'Brian, 2010, Evaluation of the regional top seal for the purpose of geologic sequestration in the Gippsland Basin, Southeastern Australia, AAPG Annual Convention & Exhibition, New Orleans, LA.

Eichhubl, P., P. S. D'Onfro, A. Aydin, J. Waters, and D. K. McCarty, 2005, Structure, petrophysics, and diagenesis of shale entrained along a normal fault at Black Diamond Mines, California—Implications for fault seal: AAPG Bulletin, v. 89, p. 1113-1137.

Engelder, T., and J. T. Leftwich Jr., 1997, A pore-pressure limit in overpressured South Texas oil and gas fields, *in* R. C. Surdam, ed., Seals, traps, and the petroleum system: AAPG Memoir 67, p. 255-267.

Espinoza, D. N., and J. C. Santamarina, 2010, Water-CO2-mineral systems: Interfacial tension, contact angle, and diffusion-Implications to CO2 geological storage: Water Resources Research, v. 46.

Færseth, R. B., E. Johnsen, and S. Sperrevik, 2007, Methodology for risking fault seal capacity: Implications of fault zone architecture: AAPG Bulletin, v. 91, p. 1231-1246.

Finkbeiner, T., M. Zoback, P. Flemings, and B. Stump, 2001, Stress, pore pressure, and dynamically constrained hydrocarbon columns in the South Eugene Island 330 field, northern Gulf of Mexico: AAPG Bulletin, v. 85, p. 1007-1031.

Firoozabadi, A., and H. J. Ramey, 1988, Surface-tension of water-hydrocarbon systems at reservoir conditions: Journal of Canadian Petroleum Technology, v. 27, p. 41-48.

Fisher, Q. J., S. D. Harris, E. McAllister, R. J. Knipe, and A. J. Bolton, 2001, Hydrocarbon flow across faults by capillary leakage revisited: Marine and Petroleum Geology, v. 18, p. 251-257.

Fisher, Q. J., and R. J. Knipe, 1998, Fault sealing processes in siliciclastic sediments: Geological Society, London, Special Publications, v. 147, p. 117-134.

Foxford, K. A., J. J. Walsh, J. Watterson, I. R. Garden, S. C. Guscott, and S. D. Burley, 1998, Structure and content of the Moab Fault Zone, Utah, USA, and its implications for fault seal prediction, *in* G. Jones, Q. J. Fisher, and R. J. Knipe, eds., Faulting, Fault Sealing and Fluid Flow in Hydrocarbon Reservoir, v. 147, London Geological Society Special Publication, p. 87-103.

Freeman, B., G. Yielding, D. T. Needham, and M. E. Badley, 1998, Fault seal prediction: the gouge ratio method: Geological Society, London, Special Publications, v. 127, p. 19-25.

Frohlich, C., 1982, Seismicity of the central Gulf of Mexico: Geology, v. 10, p. 103-106.

Frohlich, C., C. Hayward, B. Stump, and E. Potter, 2011, The Dallas-Fort Worth earthquake sequence: October 2008 through May 2009: Bulletin of the Seismological Society of America, v. 101, p. 327-340.

Galloway, W. E., 1989, Depositional framework and hydrocarbon resources of the early miocene (Fleming) episode, Northwest Gulf-Coast Basin: Marine Geology, v. 90, p. 19-29.

Galloway, W. E., T. L. Whiteaker, and P. Ganey-Curry, 2011, History of Cenozoic North American drainage basin evolution, sediment yield, and accumulation in the Gulf of Mexico basin: Geosphere, v. 7, p. 938-973.

Gibson, R. G., 1998, Physical character and fluid-flow properties of sandstone-derived fault zones: Geological Society, London, Special Publications, v. 127, p. 83-97.

Handin, J., R. V. Hager Jr., M. Friedman, and J. N. Feather, 1963, Experimental deformation of sedimentary rocks under confining pressure: AAPG Bulletin, v. 47, p. 717 - 755.

Harris, D., G. Yielding, P. Levine, G. Maxwell, P. T. Rose, and P. Nell, 2002, Using Shale Gouge Ratio (SGR) to model faults as transmissibility barriers in reservoirs: an example from the Strathspey Field, North Sea: Petroleum Geoscience, v. 8, p. 167-176.

Hickman, S. H., and M. D. Zoback, 1983, The interpretation of hydraulic fracturing pressure-time data for in situ stress determination, Hydraulic Fracturing Stress Measurements: Washington, D.C., National Academy Press.

Holtz, M. H., V. Lopez Nunez, and C. Breton, 2005, Moving Permian Basin technology to the Gulf Coast: the geologic distribution of CO2 EOR potential in Gulf Coast reservoirs: West Texas Geological Society Publication #05, v. 115, p. 11.

Hough, E. W., M. J. Rzasa, and B. B. Wood, 1951, Interfacial tensions at reservoir pressures and temperatures; apparatus and the water-methane system: AIME Petroleum Transactions, v. 192, p. 57-60.

Jaeger, J. C., and N. C. W. Cook, 1969, Fundamentals of rock mechanics (third edition): London, Chapman & Hall.

Jennings, H. Y., and G. H. Newman, 1971, Effect of temperature and pressure on interfacial tension of water against methane-normal decane mixtures: Society of Petroleum Engineers Journal, v. 11, p. 171-175.

Jev, B. I., C. H. Kaarssijpesteijn, M. Peters, N. L. Watts, and J. T. Wilkie, 1993, Akaso field, Nigeria - use of integrated 3-D seismic, fault slicing, clay smearing, and rft pressure data on fault trapping and dynamic leakage: AAPG Bulletin, v. 77, p. 1389-1404.

Jones, R. M., and R. R. Hillis, 2003, An integrated, quantitative approach to assessing fault-seal risk: AAPG Bulletin, v. 87, p. 507-524.

Kim, J. W., R. R. Berg, J. S. Watkins, and T. T. Tieh, 2003, Trapping capacity of faults in the Eocene Yegua Formation, East Sour Lake field, southeast Texas: AAPG Bulletin, v. 87, p. 415-425.

Knipe, R. J., 1997, Juxtaposition and seal diagrams to help analyze fault seals in hydrocarbon reservoirs: AAPG Bulletin, v. 81, p. 187-195.

Koledoye, B. A., A. Aydin, and E. May, 2003, A new process-based methodology for analysis of shale smear along normal faults in the Niger Delta: AAPG Bulletin, v. 87, p. 445-463.

Lander, R. H., and O. Walderhaug, 1999, Predicting porosity through simulating sandstone compaction and quartz cementation: AAPG Bulletin, v. 83, p. 433-449.

Lane, R. F., and R. C. Pace, 1998, Brazos 440-L Field, Offshore Texas: GCAGS Special Publication, p. 27-36.

Lindsay, N. G., F. C. Murphy, J. J. Walsh, and J. Watterson, 1993, Outcrop studies of shale smear on fault surfaces: International Association of Sedimentologists Special Publication, v. 15, p. 113-123.

Losh, S., E. Eglinton, M. Schoell, and J. Wood, 1999, Vertical and lateral fluid flow related to a large growth fault, South Eugene Island Block 330 field, offshore Louisiana: AAPG Bulletin, v. 83, p. 244-276.

Loveless, S., V. Bense, and J. Turner, 2011, Fault architecture and deformation processes within poorly lithified rift sediments, Central Greece: Journal of Structural Geology, v. 33, p. 1554-1568.

Lyon, P. J., P. Boult, R. R. Hillis, and S. D. Mildren, 2005, Sealing by shale gouge and subsequent seal breach by reactivation: a case study of the Zema Prospect, Otway Basin, *in* P. Boult, and J. Kaldi, eds., Evaluating Fault and Cap Rock Seals: AAPG Hedberg series, The American Association of Petroleum Geologists, p. 179-197.

Macleod, D. B., 1923, On a relation between surface tension and density: Transactions of the Faraday Society, v. 19, p. 38.

McDonnell, A., M. R. Hudec, and M. P. A. Jackson, 2009, Distinguishing salt welds from shale detachments on the inner Texas shelf, western Gulf of Mexico: Basin Research, v. 21, p. 47-59.

McDonnell, A., M. P. A. Jackson, and M. R. Hudec, 2010, Origin of transverse folds in an extensional growth-fault setting: Evidence from an extensive seismic volume

in the western Gulf of Mexico: Marine and Petroleum Geology, v. 27, p. 1494-1507.

Meckel, T., 2010, Capillary seals for trapping carbon dioxide (CO2) in underground reservoirs, *in* M. M. Matroto-Valer, ed., Developments and innovation in carbon dioxide (CO2) capture and storage technology, v. 2 Woodhead Publishing Series in Energy, p. 185-202.

Milliken, K. L., and R. M. Reed, 2002, Internal structure of deformation bands as revealed by cathodoluminescence imaging, Hickory Sandstone (Cambrian), Central Texas: Gulf Coast Association of Geological Societies Transactions, v. 52, p. 725-736.

Moos, D., and M. D. Zoback, 1990, Utilization of observations of well bore failure to constrain the orientation and magnitude of crustal stresses - application to continental, deep-sea drilling project, and ocean drilling program boreholes: Journal of Geophysical Research-Solid Earth and Planets, v. 95, p. 9305-9325.

Nagihara, S., 2010, Characterization of the sedimentary thermal regime along the Corsair growth-fault zone, Texas continental shelf, using corrected bottomhole temperatures: AAPG Bulletin, v. 94, p. 923-935.

Nicholson, A. J., S. J. Wilkins, C. Contrino, J. Termina, M. Hertz, and H. Dembicki, 2012, Fault and top seal strength at Nansen Field, East Breaks, Gulf of Mexico: AAPG Annual Convention & Exhibition.

Nicot, J. P., S. D. Hovorka, P. R. Knox, and T. Naing, 2006, Area of review: how large is large enough for carbon storage?: UIC Conference of the Groundwater Protection Council.

Ottesen Ellevset, S., R. J. Knipe, T. Svava Olsen, Q. J. Fisher, and G. Jones, 1998, Fault controlled communication in the Sleipner Vest Field, Norwegian Continental

Shelf; detailed, quantitative input for reservoir simulation and well planning: Geological Society, London, Special Publications, v. 147, p. 283-297.

Peng, D., and D. B. Robinson, 1976, New 2-constant equation of state: Industrial & Engineering Chemistry Fundamentals, v. 15, p. 59-64.

Purcell, W. R., 1949, Capillary pressures - their measurements using mercury and the calculation of permeability therefrom: AIME Petroleum Transactions, v. 186, p. 39-48.

Rainwater, E. H., 1964, Regional stratigraphy of the Gulf Coast Miocene: Gulf Coast Association of Geological Societies Transactions, v. 14, p. 81-124.

Raleigh, C. B., J. H. Healy, and J. D. Bredehoeft, 1976, Experiment in earthquake control at Rangely, Colorado: Science, v. 191, p. 1230-1237.

Sachs, W., and V. Meyn, 1995, Pressure and temperature-dependence of the surface-tension in the system natural-gas water - principles of investigation and the first precise experimental-data for pure methane water at 25-degrees-c up to 46.8-MPa: Colloids and Surfaces a-Physicochemical and Engineering Aspects, v. 94, p. 291-301.

Schowalter, T. T., 1979, Mechanics of secondary hydrocarbon migration and entrapment: AAPG Bulletin, v. 63, p. 723-760.

Seni, S. J., T. F. Hentz, W. R. Kaiser, and E. G. Wermund, eds., 1997, Atlas of northern Gulf of Mexico gas and oil reservoirs, v. 1, The University of Texas at Austin, Bureau of Economic Geology, 199 p.

Shimamoto, T., and J. M. Logan, 1981, Effects of simulated fault gouge on the sliding behavior of Tennessee Sandstone - non-clay gouges: Journal of Geophysical Research, v. 86, p. 2902-2914.

Smith, D. A., 1980, Sealing and nonsealing faults in Louisiana Gulf Coast Salt Basin: AAPG Bulletin, v. 64, p. 145-172.

Sperrevik, S., P. A. Gillespie, Q. J. Fisher, T. Halvorsen, and R. J. Knipe, 2002, Empirical estimation of fault rock properties: Norwegian Petroleum Society Special Publications, v. 11, p. 109-125.

Streit, J. E., and R. R. Hillis, 2004, Estimating fault stability and sustainable fluid pressures for underground storage of CO2 in porous rock: Energy, v. 29, p. 1445-1456.

Takahashi, M., 2003, Permeability change during experimental fault smearing: Journal of Geophysical Research-Solid Earth, v. 108.

Thomas, L. K., D. L. Katz, and M. R. Tek, 1968, Threshold pressure phenomena in porous media: Society of Petroleum Engineers Journal, v. 8, p. 174-&.

Trevino, R. H., and B. C. Vendeville, 2008, Origin of coast-perpendicular extensional faults, western Gulf of Mexico: The relationship between an early-stage ridge and a late-stage fault: AAPG Bulletin, v. 92, p. 951-964.

Tueckmantel, C., Q. J. Fisher, T. Manzocchi, S. Skachkov, and C. A. Grattoni, 2012, Two-phase fluid flow properties of cataclastic fault rocks: Implications for CO2 storage in saline aquifers: Geology, v. 40, p. 39-42.

Underschultz, J., 2007, Hydrodynamics and membrane seal capacity: Geofluids, v. 7, p. 148-158.

von Deimling, J. S., J. Greinert, N. R. Chapman, W. Rabbel, and P. Linke, 2010, Acoustic imaging of natural gas seepage in the North Sea: Sensing bubbles controlled by variable currents: Limnology and Oceanography-Methods, v. 8, p. 155-171.

Walsh, J. J., and J. Watterson, 1988, Analysis of the relationship between displacements and dimensions of faults: Journal of Structural Geology, v. 10, p. 239-247.

Watts, N. L., 1987, Theoretical aspects of cap-rock and fault seals for single-phase and 2-phase hydrocarbon columns: Marine and Petroleum Geology, v. 4, p. 274-307.

Weber, K. J., G. Mandl, W. F. Pilaar, B. V. F. Lehner, and R. G. Precious, 1978, The role of faults in hydrocarbon migration and trapping in Nigerian growth fault structures, Offshore Technology Conference, Houston, TX.

Wehr, F. L., L. H. Fairchild, M. R. Hudec, R. K. Shafto, W. T. Shea, and J. P. White, 2000, Fault seal: contrasts between the exploration and production problem, *in* M. R. Mello, and B. J. Katz, eds., AAPG Memoir 73: Petroleum Systems of South Atlantic Margins, p. 121 - 132.

Wilkins, S. J., and S. J. Naruk, 2007, Quantitative analysis of slip-induced dilation with application to fault seal: AAPG Bulletin, v. 91, p. 97-113.

Winker, C. D., and M. B. Edwards, 1983, Unstable progradational clastic shelf margins: SEPM Special Publication 33, p. 139-157.

Wiprut, D., and M. D. Zoback, 2000, Fault reactivation and fluid flow along a previously dormant normal fault in the northern North Sea: Geology, v. 28, p. 595-598.

Yielding, G., 2002, Shale Gouge Ratio - calibration by geohistory: Norwegian Petroleum Society Special Publications, v. 11, p. 1-15.

Yielding, G., P. Bretan, and B. Freeman, 2010, Fault seal calibration: a brief review: Geological Society, London, Special Publications, v. 347, p. 243-255.

Yielding, G., B. Freeman, and D. T. Needham, 1997, Quantitative fault seal prediction: AAPG Bulletin, v. 81, p. 897-917.

Zoback, M. L., and M. Zoback, 1980, State of stress in the conterminous United States: Journal of Geophysical Research, v. 85, p. 6113-6156.